Nanoscale cellular organization of viral RNA and proteins in SARS-CoV-2 replication organelles

Leonid Andronov*[1], Mengting Han*[2], Yanyu Zhu[2], Ashwin Balaji[1,5], Anish R. Roy[1], Andrew E. S. Barentine[1], Puja Patel[3], Jaishree Garhyan[3], Lei S. Qi[2,4,6,#], and W.E. Moerner[1,4,#]

[1]Department of Chemistry; [2]Department of Bioengineering; [3]In Vitro Biosafety Level 3 (BSL-3) Service Center, School of Medicine; [4]Sarafan ChEM-H; [5]Biophysics PhD Program; Stanford University, Stanford, CA 94305 U.S.A. [6]Chan Zuckerberg Biohub – San Francisco, San Francisco, CA 94158 U.S.A.

*These authors contributed equally.

#Correspondence to: W. E. Moerner, wmoerner@stanford.edu; Lei S. Qi, sqi@stanford.edu

Abstract:

The SARS-CoV-2 viral infection transforms host cells and produces special organelles in many ways, and we focus on the replication organelle where the replication of viral genomic RNA (vgRNA) occurs. To date, the precise cellular localization of key RNA molecules and replication intermediates has been elusive in electron microscopy studies. We use super-resolution fluorescence microscopy and specific labeling to reveal the nanoscopic organization of replication organelles that contain vgRNA clusters along with viral double-stranded RNA (dsRNA) clusters and the replication enzyme, encapsulated by membranes derived from the host endoplasmic reticulum (ER). We show that the replication organelles are organized differently at early and late stages of infection. Surprisingly, vgRNA accumulates into distinct globular clusters in the cytoplasmic perinuclear region, which grow and accommodate more vgRNA molecules as infection time increases. The localization of ER labels and nsp3 (a component of the double-membrane vesicle, DMV) at the periphery of the vgRNA clusters suggests that replication organelles are enclosed by DMVs at early infection stages which then merge into vesicle packets as infection progresses. Precise co-imaging of the nanoscale cellular organization of vgRNA, dsRNA, and viral proteins in replication organelles of SARS-CoV-2 may inform therapeutic approaches that target viral replication and associated processes.

Keywords: SARS-CoV-2 coronavirus, viral replication, fluorescence imaging, super-resolution fluorescence microscopy, viral RNA localization, COVID-19, viral proteins, cell infection

Introduction

Due to its global health impact, the SARS-CoV-2 betacoronavirus and its infection of mammalian cells have been the subject of a large number of studies across multiple fields. Biochemical methods have allowed researchers to investigate the interactions between the viral RNA and the host proteins *in vitro* and in cellular extracts, leading to much insight[1,2]. There have also been electron microscopy (EM) studies of resin-embedded samples as well as vitrified samples using cryo-electron tomography, all of which have been profiting from the large increase in EM resolution and contrast in recent years. These EM studies can provide very high-resolution structures of protein complexes as well as tomograms of organelles in the cellular context. High-contrast filamentous structures and membranes appear regularly in such images, allowing identification of single- and double-membrane vesicles (DMVs)[3,4,5]. However, the all-important viral RNA and associated proteins are challenging to identify by EM due to a lack of specific contrast. While some researchers have detected RNA-like filaments in vesicles[4,5], further investigations are needed to identify specific viral RNAs in the cellular context.

Fluorescence microscopy offers a highly useful and complementary set of capabilities, most importantly the specific labeling of proteins or RNA sequences. However, conventional diffraction-limited (DL) fluorescence microscopy, with its resolution constrained to ~250 nm, is unable to resolve the tiny structures that are hidden in a blurred DL image. Super-resolution (SR) microscopy based on single molecules (PALM[6], (d)STORM[7,8]) or on structured patterns of molecular depletion (STED[9], SIM[10]), however, offers far better optical resolution down to 10 nm and below. A wealth of important cellular patterns and structures has been identified in recent years, such as the banding patterns of axonal proteins in neuronal cells[11] and many others[12,13,14]. The specificity of SR imaging is useful to apply to the study of viral genomic RNA (vgRNA) and other RNA molecules; moreover, additional nanoscale imaging of critical proteins involved in coronavirus infection of cells provides crucial context for the nearby partners and surroundings of the viral RNA. In a previous proof-of-principle study, we explored the relatively safe human coronavirus 229E (HCoV-229E) from the alphacoronavirus family, which uses the APN receptor and produces only mild cold symptoms[15].

78 In this work, we apply multicolor confocal microscopy and SR microscopy to explore the
79 localization patterns of viral RNA, related viral proteins, and altered host cell structures for SARS-
80 CoV-2 betacoronavirus during the early and late infection of mammalian cells. The SARS-CoV-2
81 life cycle starts with viral entry into a host cell, facilitated by binding of viral spike protein to its
82 canonical receptor at the cell surface, the angiotensin-converting enzyme 2 (ACE2)[16], or one of
83 the alternative receptors[17]. The subsequent fusion of the viral and the host cell membranes
84 releases the viral genetic material, positive-sense single-stranded viral genomic RNA (vgRNA), into
85 the cytoplasm, where it is readily translated by host ribosomes. SARS-CoV-2 vgRNA (Fig. 1a)
86 encodes at least 29 proteins, including structural proteins that make up the virions, and non-
87 structural (NSPs) and accessory proteins that exist only within host cells and regulate various
88 processes in the intracellular viral life cycle. All NSPs originate from polyproteins that are
89 translated directly from vgRNA and are self-cleaved by viral proteases. Structural and accessory
90 proteins are translated from shorter viral genome fragments called subgenomic RNAs (sgRNAs)
91 that are transcribed from vgRNA.

92 Replication and transcription of the viral genome is carried out by the RNA-dependent RNA
93 polymerase complex (RdRp), which is assembled from nsp12 (RdRp catalytic subunit) along with
94 nsp7 and nsp8 (accessory subunits)[18]. RdRp first synthesizes either a full-length negative-sense
95 copy of vgRNA or a subgenomic negative-sense copy of vgRNA, producing double-stranded RNA
96 (dsRNA) that forms between vgRNA and the negative-sense copy. Next, using this negative-sense
97 template, a new vgRNA or an sgRNA is generated by the same polymerase enzyme. Additional
98 NSPs modify newly synthesized viral RNAs to form 5' cap structures[19] that mimic cellular mRNAs
99 to be translated by host ribosomes. The replication intermediates, such as dsRNA and uncapped
100 RNAs, might be degraded or trigger innate immune response[20] and therefore need to be
101 protected from cellular machinery. SARS-CoV-2 transforms host ER into DMVs[21] that are abundant
102 in the perinuclear region of infected cells[4,5,22] and likely encapsulate dsRNA[3,5] and newly
103 synthesized viral RNA[4,23]. However, the precise intracellular localization of replicating RdRp
104 enzymes and therefore of the replication events is not well established to date[3,23,24].

105 In this work, we focus particularly on vgRNA, dsRNA and key RdRp subunits nsp12, nsp7 and nsp8.
106 We also co-image a series of molecules, including membrane markers, nucleocapsid protein, spike

107 protein, and the nsp3 protein (reported to be a major component of a molecular pore spanning
108 both membranes of DMVs[25]), all to provide context and support for the view that vgRNA, dsRNA,
109 and RdRp act spatially in replication organelles (ROs) during viral replication. Thus, we provide
110 key information about where these important players are found in infected cells and how they
111 change with time during early *vs* late infection. Our results yield a nanoscale optical readout of
112 viral nucleic acid organization and viral proteins down to 20-40 nm during SARS-CoV-2 infection,
113 highlight the structural importance of ROs, and could potentially benefit development of future
114 therapeutic approaches.

115

116 **Results**

117 *Labeling and imaging of SARS-CoV-2 virions*

118 To specifically detect SARS-CoV-2 vgRNA, we applied RNA fluorescence *in situ* hybridization (RNA
119 FISH) with 48 antisense DNA oligonucleotide probes[26] specifically targeting the open reading
120 frame 1a (ORF1a) region which is only present in vgRNA and not in subgenomic RNAs (sgRNAs),
121 ensuring detection of only full-length viral positive-sense vgRNA (Fig. 1a). Each probe was
122 conjugated with a single blinking fluorophore for (d)STORM (direct Stochastic Optical
123 Reconstruction Microscopy)[8]. To test this labeling and imaging approach, we first imaged vgRNA
124 along with SARS-CoV-2 spike protein in purified virions (Fig. S1). While the size of SARS-CoV-2
125 virions is too small to resolve in conventional DL fluorescence microscopy (Fig. S1a), in SR the
126 internal concentric organization of the virions can be observed with vgRNA found in their center
127 and spike at the surface (Fig. S1b). The labeling efficiency with these probes is around 6
128 dyes/vgRNA in partially Proteinase K-digested virions, which was higher than in intact virions (1.7
129 dyes/vgRNA) due to poorer accessibility of their vgRNA (Fig. S1c-i).

130 Next, we imaged SARS-CoV-2 infected Vero E6 cells that were fixed at 24 hours post infection (hpi)
131 and then labeled for immunofluorescence imaging (Methods). SR microscopy of spike and
132 nucleocapsid proteins in these cells revealed assembled virions mostly at the cellular periphery,
133 often at cytoplasmic tubular projections of the plasma membrane, indicating active viral
134 production (Fig. S1j), similar to previously reported results[5,27]. These studies of virions highlight

135 the improved resolution of SR microscopy and validate the labeling approach, but much more is
136 to be learned by imaging viral RNA and proteins in the cellular interior. We now turn to the main
137 focus of this study, the intracellular replication of viral genomic RNA.

138

139 *SARS-CoV-2 genomic RNA clusters in cytoplasm of infected cells*

140 Confocal screening demonstrated three patterns of intracellular vgRNA localization (Fig. S2a):
141 scattered puncta in the cytoplasm (Type 1, Fig. 1b), appearance of bright foci in the perinuclear
142 region (Type 2, Fig. S2a), and concentration of vgRNA into large dense structures that occupy most
143 of the perinuclear region (Type 3, Fig. 1f). We find that Type 1 cells were most abundant at 6 hpi,
144 and Type 3 cells at 24 hpi, indicating that the vgRNA localization progresses from Type 1 to Type
145 3 as infection advances in time (Fig. S2b). We also find that the cell-integrated vgRNA FISH signal
146 in infected cells increases 2.2x on average from 6 to 24 hpi (Fig. S2c), representing active viral
147 replication and accumulation of vgRNA inside the cells.

148

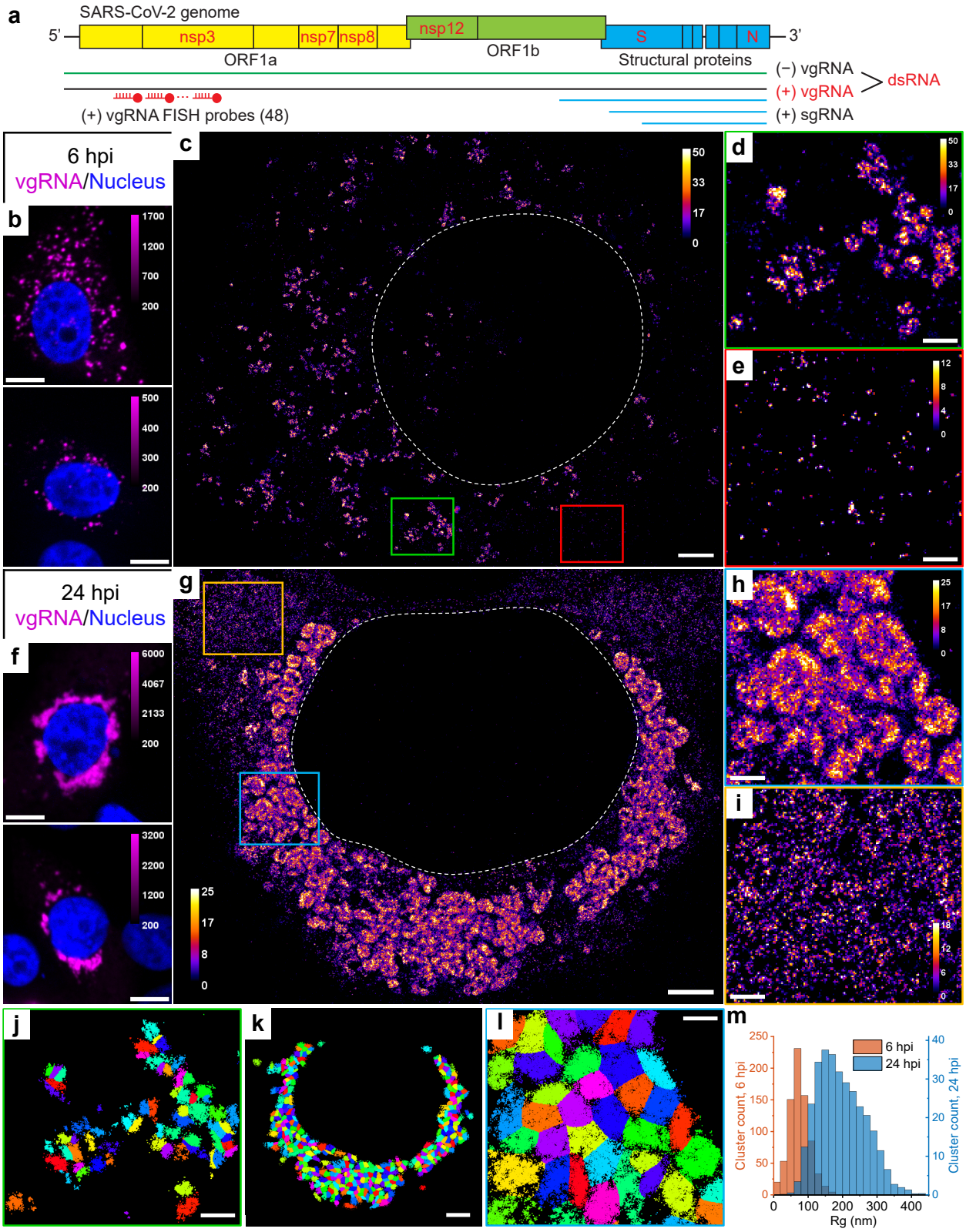

Fig. 1: Clustering of vgRNA in the cytoplasm of infected cells.

151 **a**, Scheme of SARS-CoV-2 genome with constructs used for its detection in infected cells. 48
152 antisense DNA oligonucleotide probes were used to target the ORF1a-coding region of vgRNA
153 that is exclusive to the positive-sense vgRNA and does not occur in the sgRNAs. The RNA FISH
154 probes are conjugated with AF647 or CF568. **b**, Representative confocal images of vgRNA in
155 infected Vero E6 cells at 6 hpi display scattered diffraction-limited (DL) puncta. **c**, Representative
156 SR image of an infected cell at 6 hpi reveals distinct vgRNA clusters in the cytoplasm. **d**, Zoomed-
157 in region of the SR image (green frame in **c**) displays an agglomeration of vgRNA clusters. **e**,
158 Zoomed-in region of the SR image (red frame in **c**) shows nanoscale puncta of individual vgRNA
159 molecules. **f**, Representative confocal images of vgRNA in infected Vero E6 cells at 24 hpi display
160 large DL foci in the perinuclear region of the cytoplasm. **g**, Representative SR image of an infected
161 cell at 24 hpi reveals large perinuclear vgRNA clusters. **h**, Zoomed-in region of the SR image (blue
162 frame in **g**) displays dense vgRNA clusters. **i**, Zoomed-in region of the SR image (yellow frame in
163 **g**) displays nanoscale puncta of vgRNA molecules. **j**, BIC-GMM cluster analysis of the region shown
164 in **d**. **k**, BIC-GMM cluster analysis of the cell shown in **g**. **l**, BIC-GMM cluster analysis of the region
165 shown in **h**. **m**, Histogram of the radii of gyration (Rg) of the vgRNA clusters indicate their size
166 increase between 6 hpi (magenta) and 24 hpi (green). Scale bars, 10 µm (**b**, **f**), 2 µm (**c**, **g**, **k**), 500
167 nm (**d**, **e**, **h**, **i**, **j**, **l**). Dashed lines in **c** and **g** indicate the boundary of the cell nucleus (large dark
168 region). Localizations that belong to the same cluster in **j**, **k**, **l** are depicted with the same color,
169 but colors are reused. Color bars in **c**, **d**, **e**, **g**, **h**, **i** show the number of single-molecule localizations
170 within each SR pixel (20 x 20 nm^2).

171

172 The higher spatial resolution of SR microscopy revealed that at 6 hpi (Type 1 and Type 2 cells),
173 most vgRNA localizes into clusters with an approximately round shape and a diameter of 100-
174 250 nm that scatter in the cytoplasm (Fig. 1c, d). At 24 hpi (Type 2 and Type 3 cells), the vgRNA
175 localization pattern transformed into a fascinating dense perinuclear network of approximately
176 round structures with a diameter of 300-700 nm (Fig. 1g, h). The lower number of localizations in
177 many cluster centers suggests a possibly hollow structure in these 2D images; future 3D imaging
178 can explore more aspects of the cellular localization. To quantify the transformation of vgRNA
179 clusters in infected cells, we performed a clustering analysis using a Bayesian Information
180 Criterion-optimized Gaussian Mixture Model (BIC-GMM) (Fig. 1j-l; see Methods). This analysis
181 showed an increase in the median vgRNA cluster size (Rg, radius of gyration) from 73 nm at 6 hpi
182 to 187 nm at 24 hpi (Fig. 1m), reflecting the drastic change in vgRNA localization pattern.

183 Besides dense vgRNA clusters, we observe isolated localizations of individual vgRNA molecules
184 scattered in the cytoplasm at both time points, in line with previously reported results[15,26]. These
185 appear as a haze in confocal images (Fig. S2a, Type 3) but are resolved as sparse nanoscale puncta
186 (d < 50 nm) in SR (Fig. 1e, i; Fig. S3a) which we assume to be single vgRNA copies (even though
187 the puncta are denser at 24 hpi). Using the average number of single-molecule (SM) localizations
188 per vgRNA punctum as a calibration for the number of localizations per single vgRNA, we
189 estimated the average number of vgRNA molecules in the vgRNA clusters to be around 26
190 vgRNA/cluster at 6 hpi, increasing by almost an order of magnitude to 181 vgRNA/cluster at 24
191 hpi (Fig. S3b-c; procedure detailed in Methods).

192

193 *dsRNA associates with vgRNA clusters*

194 Next, we proceeded to assess the relation of vgRNA cluster locations to viral replication. For this,
195 we immunofluorescently labeled an intermediate of coronavirus replication and transcription,
196 the hybridized dsRNA objects composed of positive-sense vgRNA and negative-sense copy, and
197 co-imaged dsRNA with vgRNA using two-color confocal and SR microscopy. In confocal
198 microscopy, dsRNA labeling was present in all cells with detectable vgRNA FISH fluorescence,
199 including in early infection, demonstrating the high sensitivity of our dsRNA immunofluorescence
200 detection (Fig. S2d). dsRNA and vgRNA appeared mostly colocalized at both time points at low
201 resolution (Fig. 2a, b), suggesting that vgRNA clusters are often found close to the replication
202 centers of SARS-CoV-2. SR microscopy revealed that dsRNA aggregates into clusters of a relatively
203 compact size (d ≈ 100-200 nm) with distinct patterns of colocalization with vgRNA at 6 or 24 hpi
204 (Fig. 2c, d).

205 To quantify the spatial relationship between dsRNA and vgRNA, we conducted pair-pair
206 correlation analysis[28]. We calculated a bivariate pair-correlation function $g_{12}(r)$, *i.e.*, the
207 distribution of the pairwise distances between the localizations of the two species[29]. The function
208 is computed only in perinuclear regions and is normalized in a way that $g_{12}(r) = 1$ for two randomly
209 and homogeneously distributed species without interaction, signifying complete spatial
210 randomness (CSR). Closely associated or colocalized species have a prevalence of short pairwise

211 distances resulting in a peak in $g_{12}(r)$ near r = 0, while anti-correlated species lack short
212 interparticle distances, which lowers $g_{12}(r)$ at r = 0 followed by peaking at r > 0.

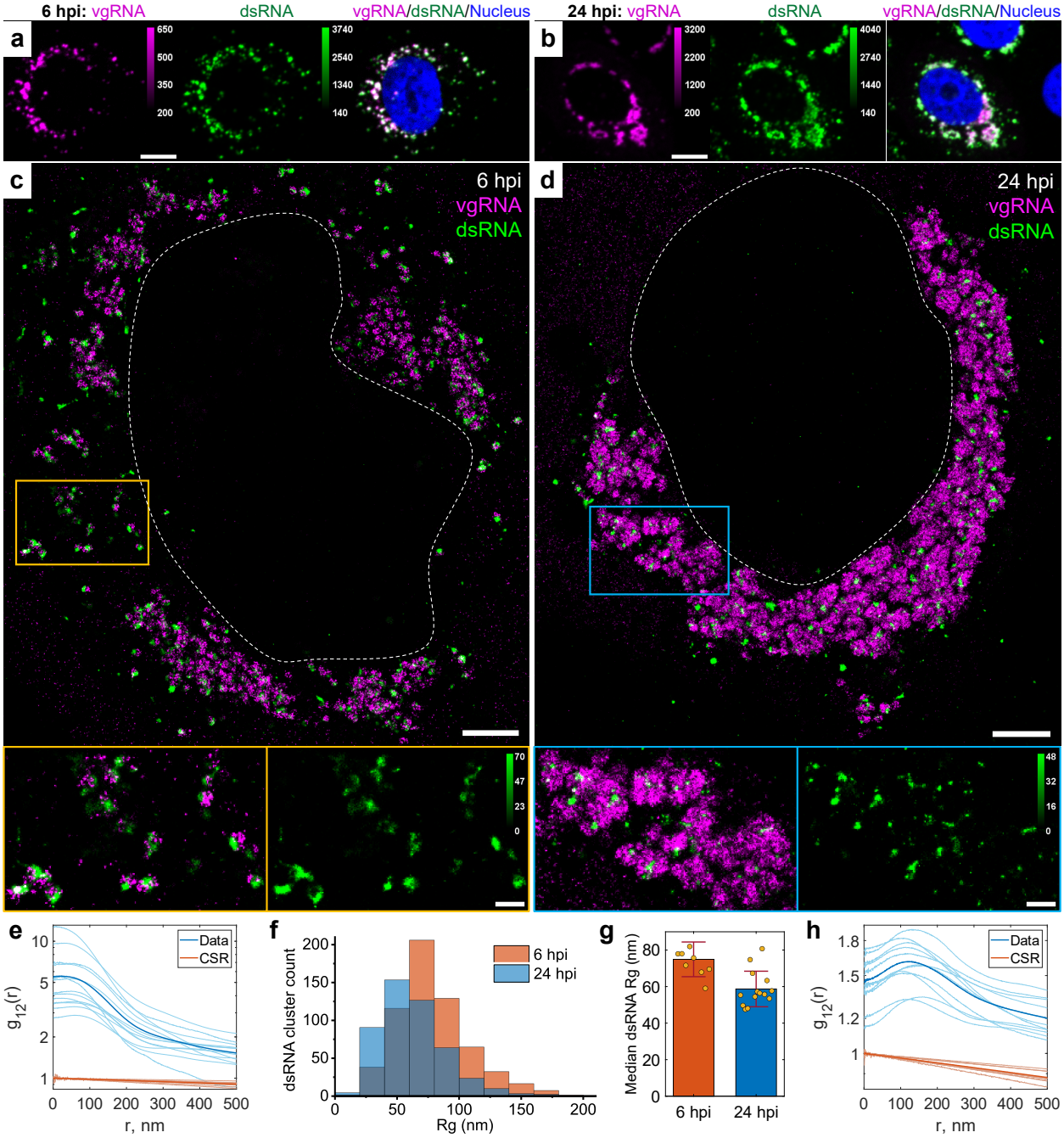

213

214 **Fig. 2: Association of dsRNA with vgRNA clusters**

215 **a**-**b**, Representative confocal images of SARS-CoV-2 infected cells display DL colocalization
216 between dsRNA (green) and vgRNA (magenta) at both 6 hpi (**a**) and 24 hpi (**b**). **c**-**d**, Representative
217 SR images of SARS-CoV-2 infected cells indicate association between dsRNA and vgRNA at 6 hpi

(**c**) and short-range anti-correlation often with concentric localization at 24 hpi (**d**). Bottom panels, zoomed-in images of corresponding colored boxes. **e**, Bivariate pair-correlation functions $g_{12}(r)$ calculated between the localizations of dsRNA and vgRNA indicate their close association at 6 hpi. **f**, Histogram of Rg of dsRNA clusters as determined by the BIC-GMM cluster analysis. **g**, Median Rg of dsRNA clusters per cell significantly decreases between 6 hpi and 24 hpi. p-value = $8 \cdot 10^{-4}$, two-tailed t-test. Error bars represent mean ± standard deviation of median Rg values of dsRNA clusters in individual cells. **h**, Bivariate pair-correlation functions $g_{12}(r)$ reveal nanoscale anti-correlation between dsRNA and vgRNA at 24 hpi. CSR, complete spatial randomness. Thin lines correspond to $g_{12}(r)$ of individual cells and bold lines are the mean values of $g_{12}(r)$ from all analyzed cells. Scale bars, 10 µm (**a**-**b**), 2 µm (**c**-**d**), 500 nm (**c**-**d**, bottom panels). Dashed lines in **c** and **d** indicate the boundary of the cell nucleus.

At early infection stages (6 hpi), dsRNA clusters appear closely associated with or adjacent to vgRNA clusters both visually and by pair-pair correlation analysis (Fig. 2c, e). By contrast, during late infection (24 hpi), dsRNA clusters anticorrelate with vgRNA at short distance scales with an average separation between them around 120 nm as indicated by bivariate pair-correlation functions $g_{12}(r)$ (Fig. 2h). Moreover, at 24 hpi, dsRNA clusters can often be found in the central voids of the large vgRNA structures (Fig. 2d), suggesting their possible concentric localization in the same ROs.

Contrary to vgRNA, the size of dsRNA clusters slightly decreases (Fig. 2f, g) and the total brightness of cellular dsRNA labeling does not significantly change between 6 hpi and 24 hpi (Fig. S2e). Interestingly, at 6 hpi but not at 24 hpi, the dsRNA signal per cell positively correlates with that of vgRNA (Fig. S2f, g). These findings indicate that the amount of dsRNA increases at early infection but reaches saturation by 24 hpi. This may suggest that after the rapid initial production of a dsRNA pool, further generation of negative-sense copies slows down and the replication shifts to the generation of vgRNA from the pool of available negative-sense templates, which is common in other coronaviruses[30].

vgRNA clusters denote the replication centers of SARS-CoV-2 genome

247 To investigate SARS-CoV-2 replication activity within the vgRNA clusters in more detail, we co-
248 imaged them with the RdRp complex, the replicating SARS-CoV-2 RNA-dependent RNA
249 polymerase[18,31], using immunofluorescent labeling of its catalytic subunit nsp12[32]. In confocal
250 images, nsp12 adopts a similar pattern as vgRNA, colocalizing with it at both 6 hpi and 24 hpi (Fig.
251 3a-b), which suggests ongoing replication at the vgRNA clusters. In SR images, nsp12 localized in
252 small sparse puncta (d < 50 nm) that were scattered within and next to the vgRNA clusters at both
253 time points (Fig. 3c-d). Because nanoscale nsp12 puncta are well separated from each other, and
254 oligomerization is not expected[18,31,33], each nanoscale punctum is likely to represent a single
255 replicating enzyme. On average, we detected 2.5 nsp12 puncta per vgRNA cluster at 6 hpi and 7.6
256 at 24 hpi (Fig. 3h).

257 From comparison of DL and SR images, one may infer fundamentally different (large-scale) nsp12
258 structures at 6 hpi and 24 hpi in confocal microscopy (Fig. 3a-b). In DL microscopy, ROs do look
259 like individual diffraction-limited dots at 6 hpi when they are sparse (Fig. 3a), *i.e.*, the average
260 distance between them is larger than the diffraction limit (even though the individual RdRp
261 complexes inside ROs are still not resolved). The same organelles when they are dense at 24 hpi
262 resemble large irregular blobs because the distance between the individual organelles becomes
263 smaller than the diffraction limit (Fig. 3b). This filling in with optically overlapping ROs creates a
264 misleading perception of distinct structures in confocal microscopy. However, SR microscopy,
265 which sees spatial details on the scale of 20-40 nm, resolves both types of structures much better.
266 The nsp12 puncta are small in both cases because they arise from individual RdRp enzymes, yet
267 the vgRNA clusters are smaller at 6 hpi and larger at 24 hpi, which is a better representation of
268 the size of these assemblies.

269 Therefore, in contrast to vgRNA but similar to dsRNA, the total cellular amount of nsp12 does not
270 significantly increase (Fig. S2h) and its nanoscale localization pattern stays the same as infection
271 progresses from 6 to 24 hpi (Fig. 3c, d). This suggests that the growth of vgRNA clusters arises
272 from a relatively constant small number of replication components between 6 and 24 hpi
273 highlighted by the constant amount of dsRNA and RdRp. Bivariate cross-correlation functions
274 calculated between nsp12 and vgRNA localizations peaked at 0 nm indicating association of these
275 two targets at both 6 and 24 hpi (Fig. 3i). Since vgRNA clusters colocalize with the catalytic subunit

of RdRp, we suggest that vgRNA clusters combined with the nearby RdRp enzymes and dsRNA highlight ROs that act as centers for replication and transcription of SARS-CoV-2.

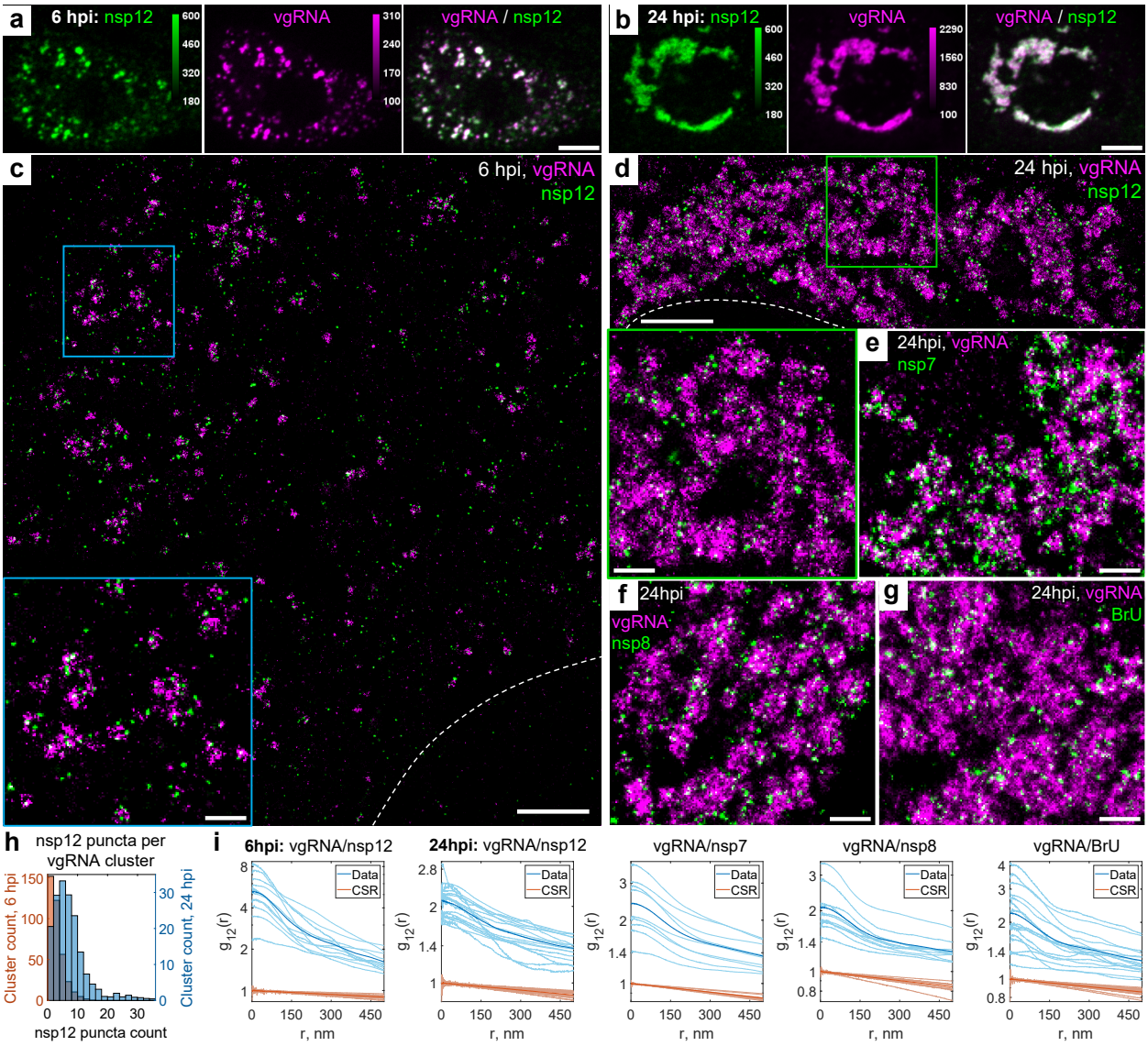

Fig. 3: Association of SARS-CoV-2 replication enzyme with vgRNA clusters

a-**b**, Representative confocal images of SARS-CoV-2 infected cells display DL colocalization between nsp12, the catalytic subunit of RdRp (green) and vgRNA (magenta) at both 6 hpi (**a**) and 24 hpi (**b**). **c**-**d**, Representative SR images of SARS-CoV-2 infected cells indicate nanoscale association between nsp12 and vgRNA at both 6 hpi (**c**) and 24 hpi (**d**). Insets show magnified images of corresponding regions in the colored boxes. **e**-**f**, Representative SR images of vgRNA with nsp7 (**e**) or nsp8 (**f**) in the perinuclear regions of SARS-CoV-2 infected cells indicate association of nsp7 and nsp8 with vgRNA clusters. **g**, Representative SR image of vgRNA with

287 newly synthesized viral RNAs labeled by BrU in a SARS-CoV-2 infected cell indicates localization of
288 newly synthesized viral RNAs within the perinuclear clusters of vgRNA. **h**, Number of nanoscale
289 puncta of nsp12 per vgRNA cluster. **i**, Bivariate pair-correlation functions for vgRNA and nsp12,
290 nsp7, nsp8 and newly transcribed viral RNA labeled with BrU peak at r = 0 nm indicating
291 association between these target pairs. Scale bars, 10 µm (**a**-**b**), 2 µm (**c**-**d**), 500 nm (**e**-**g** and insets
292 in **c**-**d**). Dashed lines in **c** and **d** indicate the edge of the cell nucleus.

293

294 To verify that nsp12 labeling is a good reporter of assembled replication complexes, we have also
295 imaged two accessory subunits of RdRp, nsp7 and nsp8. We find close association of these
296 subunits with vgRNA as shown in Fig. 3e, f, and in the pair-correlation functions of Fig. 3i (see also
297 Fig. S4 and S5). Nsp12 and nsp8 colocalized with each other on the nanoscale (Fig. S6), indicating
298 their interaction within ROs, as expected for subunits of assembled RdRp.

299 Finally, to confirm that the vgRNA clusters we observe contain newly replicated viral RNA, we
300 provided brominated uridine (BrU) to the infected cells in the form of 5-bromouridine 5'-
301 triphosphate (BrUTP) for 1 hour before fixation while endogenous transcription was inhibited by
302 actinomycin D[34,35]. Immunofluorescent labeling of BrU then highlights newly replicated RNA.
303 Confocal and SR imaging localizes RNA-containing BrU to the perinuclear clusters of vgRNA (Fig.
304 3g, Fig. S7) and close to nsp12 (Fig. S8), further proving that these structures are the sites of active
305 replication and transcription of viral RNA.

306

307 *vgRNA clusters are enclosed in ER-derived membranous organelles*

308 Coronaviruses are known to transform the host ER into replication-permissive structures, such as
309 convoluted membranes and DMVs[3,22,36]. To investigate the relation of vgRNA clusters with cellular
310 ER, we immunofluorescently labeled Sec61β, an ER membrane protein[37], in Vero E6 cells stably
311 expressing Sec61β-GFP[15]. Confocal images of these cells show the appearance of Sec61β spots
312 that colocalize with vgRNA against the mostly unaltered ER background at 6 hpi (Fig. 4a). At
313 24 hpi, however, substantial amounts of Sec61β accumulate close to the perinuclear vgRNA
314 clusters, while the ER tubules outside these regions become poorly visible (Fig. 4a), consistent

with the virus-induced rearrangement of the ER and the inhibition of host gene expression by SARS-CoV-2[38].

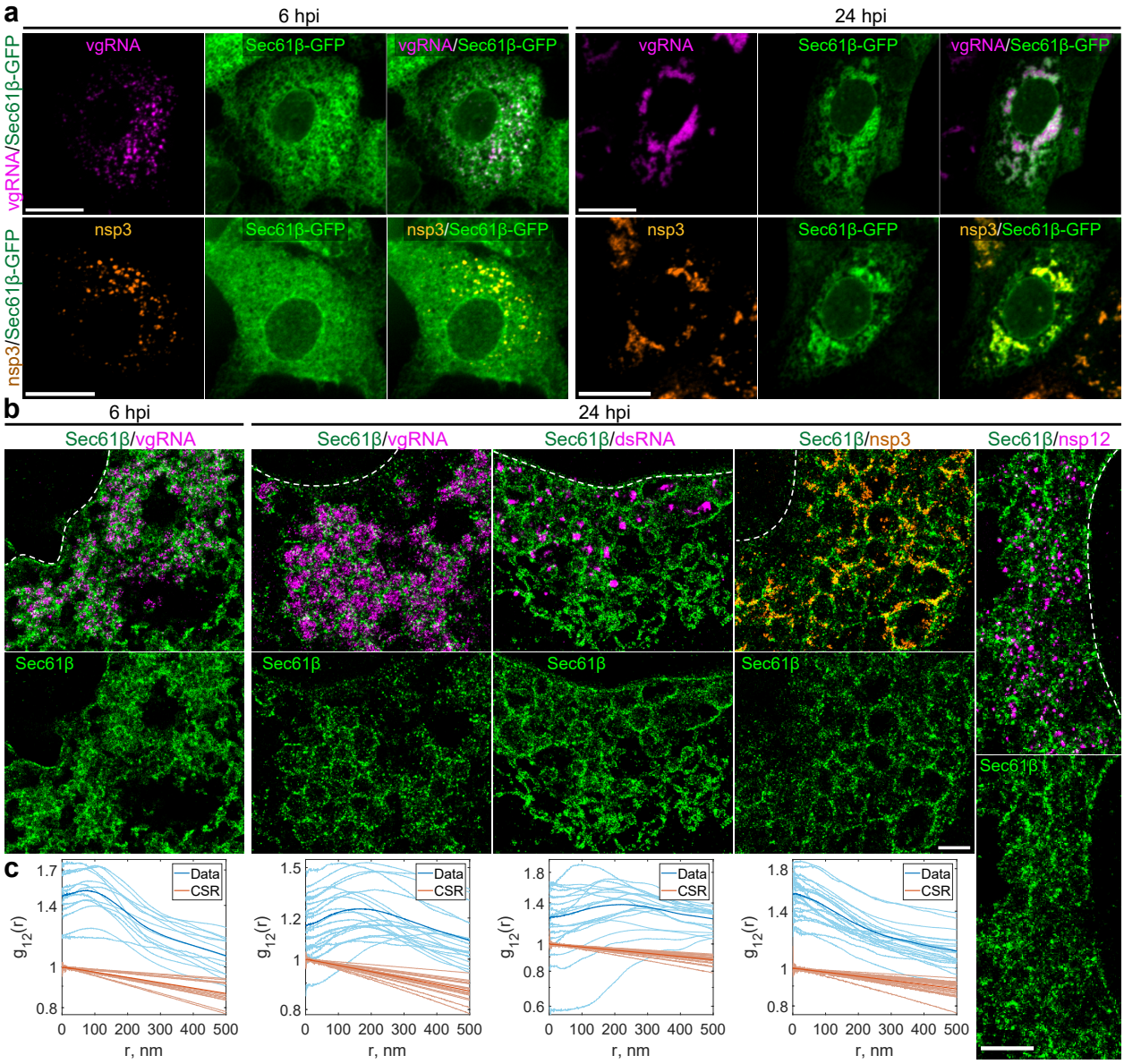

Fig. 4: vgRNA clusters are encapsulated in membranes of remodeled ER

a, Representative confocal images of SARS-CoV-2 infected cells indicate an appearance of dense perinuclear foci of Sec61β ER labeling (green) at 24 hpi that colocalizes with vgRNA and nsp3. **b**, SR images reveal concentric organization of Sec61β around vgRNA, dsRNA and nsp12, and colocalization of Sec61β with nsp3. **c**, Bivariate pair-correlation functions indicate anti-correlation of Sec61β with vgRNA and dsRNA and association of Sec61β with nsp3. Scale bars, 20 µm (**a**) and 1 µm (**b**). Dashed lines in **b** indicate the boundary of the cell nucleus.

325 In SR, we observe encapsulation of the vgRNA clusters by ring-like structures of the altered ER at
326 6 hpi (Fig. 4b, Fig. S9). As infection progresses, the ER-derived ring- or sphere-like structures grow
327 to accommodate larger vgRNA clusters at 24 hpi (Fig. 4b, Fig. S10). Pair-correlation functions peak
328 at the distance of the typical radius of vgRNA clusters indicating nanoscale anti-correlation
329 compatible with the ER-derived encapsulation of vgRNA (Fig. 4c). dsRNA (Fig. 4b, Fig. S11) and
330 nsp12 (Fig. 4b) are also found to be encapsulated by the same remodeled ER membranes
331 suggesting that vgRNA, dsRNA and RdRp are all located within the same ER-derived ROs.

332 To further confirm that these clusters are surrounded by membranes, we used a (d)STORM-
333 compatible general membrane marker CellMask Deep Red[39]. This dye broadly stains cellular
334 membranes, including the nuclear envelope, mitochondrial membranes, and SARS-CoV-2 virions
335 at the plasma membrane (Fig. S12). The nanoscale image contrast with CellMask Deep Red is
336 poorer than specific protein labeling of the Sec61β ER label due to background from membranes
337 of different cellular organelles. Nevertheless, in the perinuclear region of infected cells, we
338 observed the appearance of a complex membranous network that anti-correlates with vgRNA
339 and dsRNA, with visible encapsulation of vgRNA and dsRNA clusters (Fig. S12, S13). Taken
340 together, these findings indicate that each vgRNA-dsRNA-RdRp cluster is located inside a
341 membrane-bound RO that originates from altered host ER transformed by SARS-CoV-2.

342

343 *Nsp3, spike and nucleocapsid proteins localize at the surface of SARS-CoV-2 replication organelles*

344 Because the nsp3 protein of betacoronaviruses is essential for the DMV formation[21,40], and nsp3
345 is a constituent of a DMV molecular pore[25], we proceeded to localize this non-structural protein
346 to relate the ROs to the SARS-CoV-2-induced DMVs. At DL resolution, nsp3 labeling adopts a
347 pattern that colocalizes with vgRNA at both 6 and 24 hpi, similar to dsRNA and nsp12 (Fig. 5a, f).
348 SR imaging of these cells, however, revealed striking nanoscale positioning of nsp3. At 6 hpi,
349 sparse nsp3 can be found surrounding isolated vgRNA clusters (Fig. 5b, c), while larger nsp3
350 aggregates are situated amidst bunched vgRNA clusters (Fig. 5d). At 24 hpi, nsp3 localizes at the
351 borders of the large vgRNA clusters, encircling them in incomplete rings and forming a partial

perinuclear network (Fig. 5g-i). Similar nsp3 arrangements can be observed in relation to dsRNA (Fig. S14).

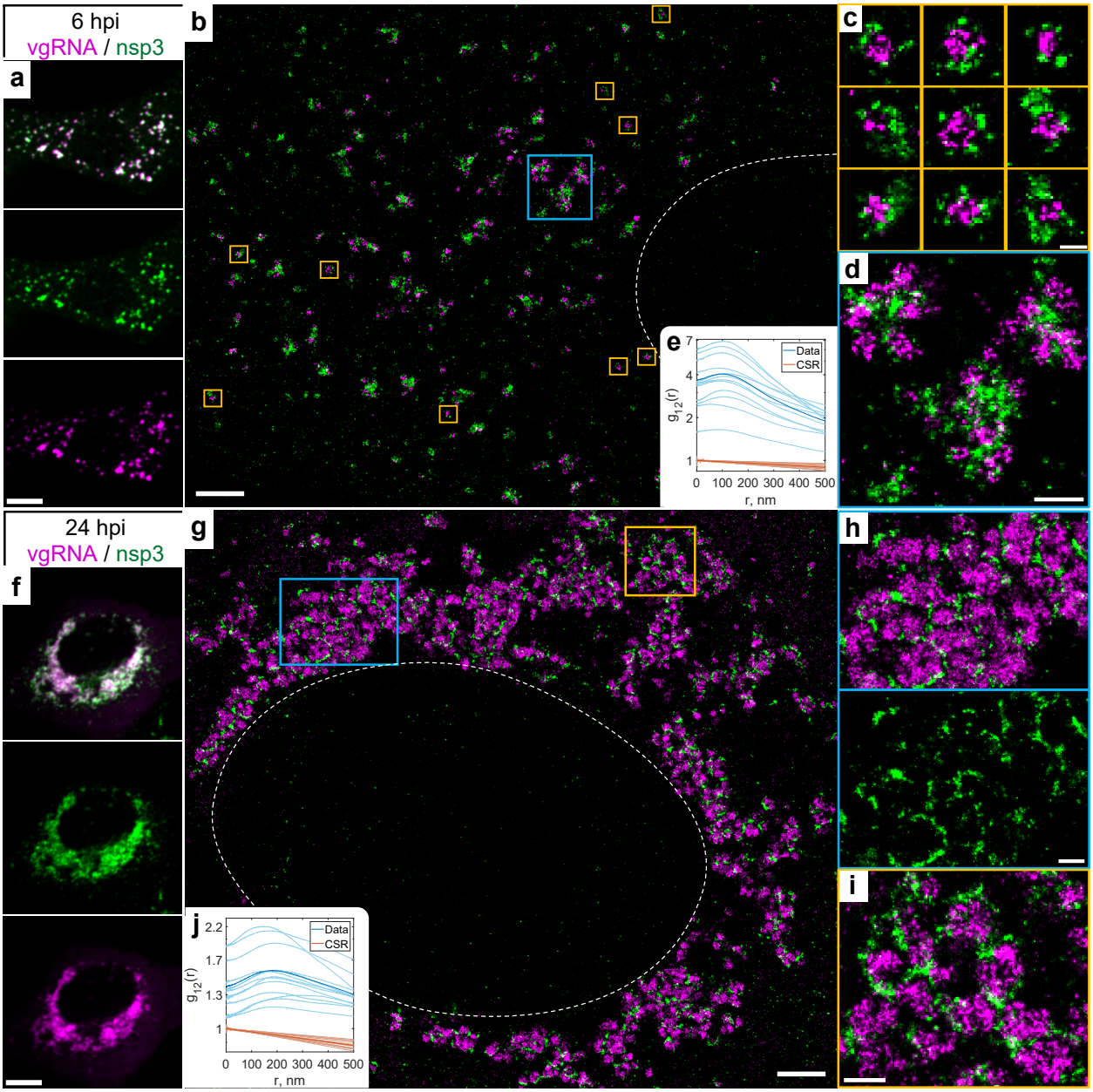

Fig. 5: Nsp3 localizes at the surface of vgRNA clusters

a, Representative confocal images of a SARS-CoV-2 infected cell display DL colocalization between punctate vgRNA (magenta) and nsp3 (green) labeling at 6 hpi. **b**, Representative SR image of a SARS-CoV-2 infected cell at 6 hpi. **c**, Zoomed-in images of selected vgRNA particles (yellow boxes in **b**) indicate the localization of nsp3 at the surface of the vgRNA clusters. **d**, Magnified region with aggregates of vgRNA clusters (blue box in **b**) displays dense nsp3 localization in the core of

361 these aggregates. **e**, Bivariate pair-correlation functions calculated between the SM localizations
362 of vgRNA and nsp3 indicate nanoscale anti-correlation of these targets at 6 hpi. **f**, Confocal images
363 show that vgRNA and nsp3 occupy approximately the same regions in a SARS-CoV-2 infected cell
364 at 24 hpi. **g**, Representative SR image of a SARS-CoV-2 infected cell at 24 hpi. **h**-**i**, Magnified regions
365 of the SR image (colored boxes in **g**) reveal that nsp3 localizes in interstitial regions or
366 encapsulates vgRNA clusters. **j**, Bivariate pair-correlation functions indicate nanoscale anti-
367 correlation between vgRNA and nsp3 at 24hpi. Scale bars, 10 µm (**a**, **f**), 2 µm (**b**, **g**), 500 nm (**d**, **h**,
368 **i**), 200nm (**c**). Dashed lines in **b**, **g** indicate the boundary of the cell nucleus.

369

370 The anti-correlation of vgRNA with nsp3 and dsRNA with nsp3 (Fig. 5, Fig. S14) closely resemble
371 the pattern observed with vgRNA and dsRNA with Sec61β (Fig. 4, Fig. S11), suggesting that nsp3
372 may also be localized at the ER-derived membranous surface of the ROs. To further confirm this
373 hypothesis, we co-imaged nsp3 with Sec61β and CellMask (Fig. 4, Fig. S13, S15). The SR images
374 and the pair-correlation analysis indicated colocalization between nsp3 and both membrane
375 markers at both time points (Fig. 4b-c, Fig. S13, S15), confirming that nsp3 localizes on the
376 membranes encircling the SARS-CoV-2 ROs.

377 Besides these characteristic localization patterns of nsp3, we observed a few cells with two
378 different phenotypes at 24 hpi, one with an ER-like network that occupies large regions in the
379 cytoplasm (Fig. S16a), and another one with nsp3 densely diffused throughout the whole
380 cytoplasm (Fig. S16b). The ER-like network may represent nsp3 proteins being heavily translated
381 on ER membranes, while nsp3 proteins found outside the perinuclear region are less likely to be
382 associated with the SARS-CoV-2 replication process and might represent other nsp3 functions,
383 such as a papain-like proteolytic function[41] or post-translational modification of host proteins[42],
384 which can become objects of future SR studies.

385 The localization of nsp3 at the surface of isolated vgRNA-dsRNA clusters at 6 hpi is consistent with
386 the localization of molecular pores on the DMV membrane observed by cryo-EM[25]. At late
387 infection times, DMVs have been observed to merge into vesicle packets (VPs)[5] that are also likely
388 to contain pores, however molecular pores in the VP membranes have not yet been studied in
389 detail to our knowledge. Nevertheless, previous studies report that in late infection the
390 perinuclear region becomes filled with DMVs and VPs[22] that strongly resemble the ROs reported

391 here. The size of vgRNA clusters at 6 hpi and at 24 hpi from our data is similar to the previously
392 reported size of DMVs and VPs, correspondingly[5].

393 To search for a possible role of perinuclear vgRNA clusters in virion assembly, we co-imaged
394 vgRNA with two SARS-CoV-2 structural proteins, spike and nucleocapsid (Fig. S17, S18). Spike
395 labeling forms typical ~ 150 nm hollow particles at the cell periphery, and we detect weak vgRNA
396 signal in the center of some of these particles (Fig. S17b), consistent with the structure of SARS-
397 CoV-2 virions that contain a single vgRNA molecule. Inside the host cells, spike localizes at the
398 nuclear envelope and in some cytoplasmic organelles; however, it is mostly excluded from the
399 perinuclear vgRNA clusters (Fig. S17a, c). Nucleocapsid protein demonstrates rather diffuse
400 localization throughout the cytoplasm, in accordance with its function in the formation of SARS-
401 CoV-2 ribonucleocapsid complexes[43], but is also excluded from the RO interior (Fig. S18a).
402 Nevertheless, in the perinuclear region we detect sparse localizations of both spike and
403 nucleocapsid proteins next to the vgRNA clusters and between them, likely at the DMV
404 membranes, as highlighted by anti-correlation of these proteins with vgRNA at $r < 200$ nm (Fig.
405 S17c, S18b), similar to the nsp3/vgRNA and Sec61β/vgRNA pairs. The localization of nucleocapsid
406 protein at the RO membranes has already been reported[44], and spike protein has a
407 transmembrane domain[45] and tends to localize not only to virion membranes, but also to
408 intracellular membranes, such as the nuclear envelope (Fig. S17a); therefore, small amounts of
409 spike can also be present at RO membranes. Our SR data suggests that while the vgRNA clusters
410 are not directly involved in SARS-CoV-2 virion assembly, it is possible that early stages of virion
411 assembly start at the RO membrane, once vgRNA molecules leave the ROs.

412 Taken together, our results provide evidence that vgRNA accumulates in DMVs at 6 hpi and in VPs
413 at 24 hpi. dsRNA clusters occur within the same vesicles but occupy distinct parts of them
414 compared to vgRNA. Our data suggests a model (Fig. 6) where SARS-CoV-2 RNA is replicated and
415 transcribed within these DMVs and VPs as highlighted by the proximal localizations of RdRp.

416

417 **Discussion**

418 Previous biochemical and EM studies allowed researchers to build models of the intracellular life
419 cycle of SARS-CoV-2[24,46,47]; however, precise localization of specific viral proteins and RNA
420 molecules is challenging due to lack of specific contrast in EM and low resolution in DL
421 fluorescence microscopy. SR fluorescence microscopy is well suited for coronavirus studies in cells
422 as it provides both specific contrast and high resolution (~20 nm and below depending upon
423 photons collected[48]). However, to date few studies have employed this method for coronavirus
424 biology[15], with even less focus on SARS-CoV-2[36,44,49], and none of them addressed the SARS-CoV-
425 2 replication process in detail. Here we apply SR fluorescence microscopy to precisely localize the
426 key players of SARS-CoV-2 replication at different time points in infected cells. Building upon a
427 previously developed method for simultaneous labeling of coronavirus vgRNA with dsRNA and
428 protein immunofluorescence[15], and using improved fixation and multi-color SR imaging protocols
429 (see Methods), we obtain and quantify the appearance and molecular compositions of ROs of
430 SARS-CoV-2 in cells at different stages of infection.

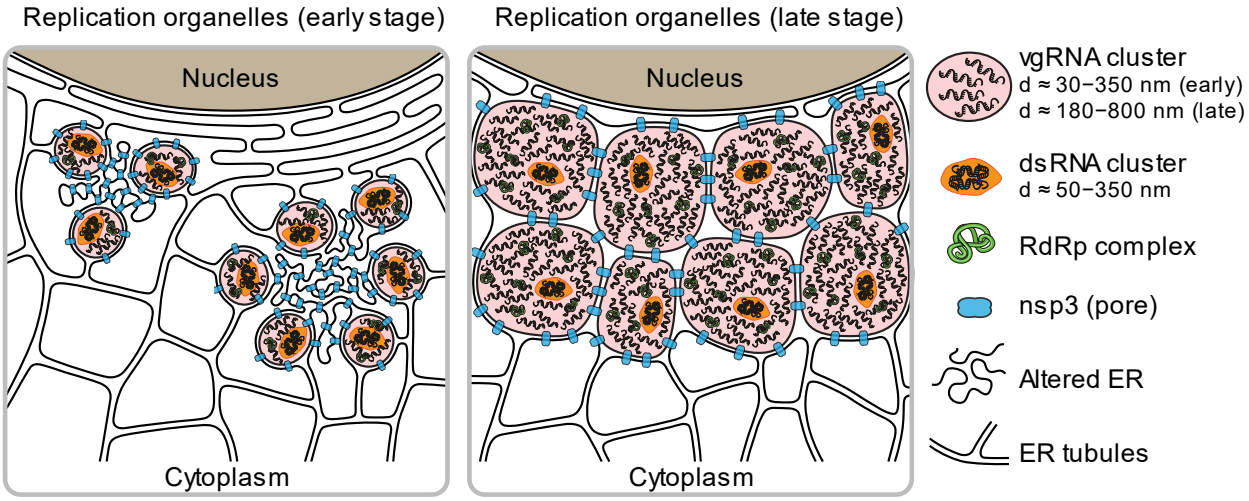

431

432 **Fig. 6: Proposed model for SARS-CoV-2 replication organelles containing various RNA and**
433 **protein molecules at early and late stages of infection.**

434

435 In this study, our results taken together depict a compelling and novel picture of ROs containing
436 various molecules including vgRNA, dsRNA, RdRp, nsp3, and ER membrane (Fig. 6). In this model,
437 we compare the organization of ROs at early and late stages of infection and show how specific
438 RNA and protein molecules are spatially organized in ROs. Compared to the simpler and less

439 pathogenic HCoV-229E case, SARS-CoV-2 appears to generate more complex clusters of vgRNA,
440 and with the imaging of viral proteins involved in vgRNA replication and in DMV formation, the
441 structural importance of ROs is now clear.

442 The detailed intracellular localization of the central SARS-CoV-2 component, vgRNA, has remained
443 vague in the literature. Our RNA FISH method[15] targets specific sequences in vgRNA (Fig. 1a) and
444 detects single vgRNA molecules (Fig. 1e, i; Fig. S1, S3a, S17b), allowing counting of the number of
445 vgRNA molecules within specific regions (Fig. S3b-c). We find for the first time that most cellular
446 vgRNA localizes into dense clusters of an approximately round shape that grow and migrate to
447 the perinuclear region as infection time increases. We show that these clusters appear confined
448 in membranous vesicles derived from ER as emphasized by the localization of Sec61β and
449 CellMask at their surface (Fig. 4b, Fig. S9-S13). From comparison with earlier EM images[5,22,25] and
450 from nsp3 localization at their surface[25] (Fig. 5), we can conclude that these vesicles are most
451 likely DMVs at an early-mid infection time that grow and merge into VPs as infection progresses.

452 Previously, metabolic radioactive labeling was used to localize newly synthesized RNA in SARS-
453 CoV-1 and MERS-CoV-infected cells to DMVs[4]. However, metabolic labeling only localizes a
454 fraction of vgRNA molecules with little sequence specificity and with a background of viral sgRNA.
455 Here, we specifically label vgRNA of SARS-CoV-2 for SR microscopy and show that it also localizes
456 in patterns that suggest confinement in DMVs, consistent with the earlier findings on SARS-CoV-
457 1 and MERS-CoV[4]. Our metabolic labeling of infected cells with BrUTP also localized newly
458 synthesized viral RNAs to the perinuclear vgRNA clusters (Fig. 3g, Fig. S7), which agrees with
459 earlier results[4,23,34] and solidifies our conclusions on the spatial localization of vgRNA and viral
460 replication machinery inside DMVs.

461 Previous studies also suggested the presence of dsRNA in DMVs of SARS-CoV-1[3] and SARS-CoV-
462 2[5]. EM images of DMVs often display a complex filamentous network in their interior that was
463 attributed to viral RNA molecules[5]. However, the exact type of these RNAs was not determined
464 due to the absence of specific labeling. As one might expect, single-stranded vgRNA can form a
465 secondary structure that includes many short dsRNA fragments *e.g.*, in stem loops[50,51]. This makes
466 it difficult to distinguish between viral dsRNA and vgRNA by measuring the diameter of the

467 filaments, taking into account that the detection probability of ssRNA might be lower due to a
468 decreased EM contrast for ssRNA than for dsRNA. Reported abundant branching of filaments in
469 DMVs[5], however, is typical for ssRNA secondary structures[52]. Indeed, these references present
470 some evidence about the presence of both dsRNA and vgRNA in DMVs; however, to our
471 knowledge, there was no simultaneous observation of both vgRNA and dsRNA within the same
472 DMVs.

473 Here we use the J2 anti-dsRNA antibody that recognizes only long dsRNA fragments (≥ 40bp) with
474 no detection of the ssRNA secondary structures[53,54]. The J2 antibody has been reported to
475 underestimate dsRNA localization[26]; however, using optimized antibody concentrations (Fig. S19,
476 S20) and optimized staining protocols as detailed in Methods, we achieved excellent sensitivity
477 to dsRNA with signal present in all infected cells, even in early infection with very low vgRNA
478 levels (Fig. S2d). Our two-color SR imaging revealed for the first time that most dsRNA and vgRNA
479 are located within the same DMVs and VPs, occupying distinct regions of these vesicles, and
480 adopting an anti-correlation pattern at short distances (r < 100 nm) at 24 hpi (Fig. 2). Another
481 novel observation is the relatively constant amount of dsRNA and a slight decrease in dsRNA
482 cluster size between 6 and 24 hpi despite the huge change in the vgRNA landscape (Fig. 2, Fig.
483 S2c, e).

484 It has been proposed that the RdRp complex of SARS-CoV-1 is located at convoluted membranes
485 and inside DMVs based on immunogold labeling of nsp8[3]. However, nsp8 has intracellular
486 functions other than as an RdRp accessory subunit[55,56] that might be exercised at the convoluted
487 membranes. Here we label the catalytic RdRp subunit, nsp12[18], and find that it mostly localizes
488 to the vgRNA clusters at both 6 and 24 hpi (Fig. 3a-d, i), suggesting that SARS-CoV-2 replication
489 and transcription occur preferentially in the vgRNA-filled ROs, where dsRNA resides as well.
490 Additional experiments revealed that two other RdRp subunits, nsp7 and nsp8, as well as newly
491 synthesized viral RNA also localize to the vgRNA clusters (Fig. 3e-g, i; Fig. S4-S8), further proving
492 the role of these clusters as replication organelles.

493 Nsp3 of betacoronaviruses (SARS-CoV-1, MERS-CoV and MHV) was previously localized to the
494 convoluted membranes and to the DMV membranes using immuno-EM[3,4,57,58] and cryo-ET[25];

495 however, these studies were limited to early-mid infection at 8-12 hpi. In our study, we report
496 two localization patterns of nsp3 of SARS-CoV-2 at 6hpi: 1) sparse nsp3 at the surface of isolated
497 vgRNA-dsRNA clusters (Fig. 5c, Fig. S14a); and 2) dense nsp3 within the accumulations of vgRNA-
498 dsRNA clusters (Fig. 5d, Fig. S14a). While the first pattern most likely corresponds to the RO/DMV
499 membranes considering the role of nsp3 as a DMV pore[25], the second one resembles a pattern
500 found in other coronaviruses that was attributed to the convoluted membranes[3,4,59]. Convoluted
501 membranes are typically found within dense groups of DMVs in early-mid infection[3,4] and
502 localization of nsp3 on them might represent early steps of viral transformation of ER into DMVs.
503 We found this nsp3 pattern anti-correlated with vgRNA (Fig. 5d, e) and with dsRNA (Fig. S14a, b),
504 suggesting little to no vgRNA or dsRNA at the convoluted membranes, in line with previous studies
505 on other coronaviruses[4].

506 At 24 hpi, we did not observe these early infection patterns of nsp3 localization. Instead, we show
507 for the first time that at 24 hpi, nsp3 densely localizes at the membranes that separate large
508 vgRNA clusters and grows into a considerable perinuclear network that contains the ROs (Fig. 5g-
509 i, Fig. S14c). Since the molecular pores of VPs have not yet been investigated in detail, we can
510 speculate that this late infection nsp3 pattern corresponds to the pores of VPs that should also
511 be much denser than those of isolated DMVs, considering the increased density of nsp3 labeling.
512 Additional rare phenotypes of nsp3 localization that we also report for the first time (Fig. S16)
513 illustrate the variability of SARS-CoV-2 infection course and should lead to further research on the
514 other intracellular functions of this viral protein.

515 Taken together, we investigated several key factors of SARS-CoV-2 replication: vgRNA, dsRNA,
516 RdRp and nsp3 inside infected cells with SR microscopy for the first time. We discovered and
517 characterized the nanoscale structure of perinuclear clusters of vgRNA and demonstrated by
518 RdRp labeling that they associate with SARS-CoV-2 ROs. We found that the ROs also contain
519 dsRNA and are encapsulated in ER-derived membranes. Using SR data on nsp3, we conclude that
520 these virus-induced organelles correspond to DMVs.

521 This study expands the knowledge of the biology of coronaviruses and opens new possibilities for
522 therapeutics against SARS-CoV-2, considering that clusters of vgRNA have also been reported in

523 SARS-CoV-2 infected interstitial macrophages of human lungs[17], suggesting their importance in
524 COVID-19. Careful examination of the organization of ROs may provide new avenues to target the
525 organelles to disrupt SARS-CoV-2 replication and transcription. Examining localization patterns for
526 different viral variants or in different host cells will be useful to broaden understanding of the viral
527 infection. It will also be important to examine how the structures reported in this study change
528 upon the addition of drug treatments. Our imaging approach may also offer insights into long
529 COVID by investigating cells that are infected by SARS-CoV-2 that may still contain RO-like
530 structures after symptoms disappear.

531

532 **Methods**

533 *Antibodies*

534 Primary antibodies and the optimal dilutions and concentrations used are as follows: goat
535 polyclonal anti-spike S2 (Novus Biologicals, AF10774-SP, 1:20, 10 µg/mL), mouse monoclonal anti-
536 dsRNA (SCICONS, 10010200, 1:200, 5 µg/mL), rabbit polyclonal anti-RdRp/nsp12 (Sigma-Aldrich,
537 SAB3501287-100UG, 1:500, 2 µg/mL), mouse monoclonal anti-nucleocapsid (Thermo Fisher,
538 MA5-29981, 1:500, 2 µg/mL), rabbit polyclonal anti-nsp3 (Thermo Fisher, PA5-116947, 1:134, 5
539 µg/mL), sheep polyclonal anti-GFP (Bio-Rad, 4745-1051, 1:1000, 5 µg/mL), rabbit polyclonal anti-
540 GFP (Novus Biologicals, NB600-308SS, 1:163, 5 µg/mL), rabbit monoclonal anti-nsp7 (GeneTex,
541 GTX636719, 1:200, 2 µg/mL), mouse monoclonal anti-nsp8 (GeneTex, GTX632696, 1:134,
542 5 µg/mL), mouse monoclonal anti-BrdU (Thermo Fisher, B35128, 1:50, 2 µg/mL). Secondary
543 antibodies and the optimal dilutions and concentrations used are as follows: AF647-conjugated
544 donkey anti-mouse IgG (Thermo Fisher, A-31571, 1:500, 4 µg/mL), AF647-conjugated donkey anti-
545 rabbit IgG (Thermo Fisher, A-31573, 1:500, 4 µg/mL), AF647-conjugated donkey anti-sheep IgG
546 (Thermo Fisher, A-21448, 1:500, 4 µg/mL), CF568-conjugated donkey anti-goat IgG (Sigma-
547 Aldrich, SAB4600074-50UL, 1:500, 4 µg/mL), CF568-conjugated donkey anti-rabbit IgG (Sigma-
548 Aldrich, SAB4600076-50UL, 1:500, 4 µg/mL), CF568-conjugated donkey anti-mouse IgG (Sigma-
549 Aldrich, SAB4600075-50UL, 1:500, 4 µg/mL), CF568-conjugated donkey anti-sheep IgG (Sigma-
550 Aldrich, SAB4600078-50UL, 1:500, 4 µg/mL), CF583R-conjugated donkey anti-mouse IgG (Custom
551 CF Dye, lot 23C1122, Biotium, 1:250, 4 µg/mL), CF583R-conjugated donkey anti-rabbit IgG
552 (Custom CF Dye, lot 23C0811, Biotium, 1:250, 4 µg/mL). To confirm that the fluorophore attached
553 to the secondary antibody does not produce artifacts, in a number of cases we switched the labels
554 by switching the secondary antibodies, and found no difference in the SR structures observed.

555

556 *Culture of cell lines*

557 The Vero E6 cells (African green monkey kidney epithelial cells, ATCC, CRL-1586), HEK293T cells
558 (human embryonic kidney epithelial cells, ATCC, CRL-3216), and Vero E6-TMPRSS2 cells were
559 cultured in Dulbecco's modified Eagle medium (DMEM) with GlutaMAX, 25 mM D-Glucose, and

560 1 mM sodium pyruvate (Gibco, 10569010) in 10% FBS (Sigma-Aldrich, F0926) at 37°C and 5% CO2
561 in a humidified incubator. Cell lines were not authenticated after purchase prior to use. For Vero
562 E6-TMPRSS2, Geneticin (G418) was added at a final concentration of 1mg/ml.

563

564 *Lentivirus production for ER labeling with Sec61β*

565 To produce lentivirus, HEK293T cells were cultured in 10-cm dishes and transiently transfected
566 with 9 µg lentiviral plasmid pLV-ER-GFP (Addgene, 80069, a gift from Pantelis Tsoulfas), 8 µg
567 pCMV-dR8.91, and 1 µg PMD2.G packaging plasmids using 25 µL TransIT-LT1 Transfection Reagent
568 (Mirus, MIR 2306). After 72 h of transfection, supernatant was filtered through 0.45 µm filters,
569 concentrated using Lentivirus Precipitation Solution (ALSTEM, VC100) at 4°C overnight, and
570 centrifuged at 1,500x g for 30 min at 4°C to collect virus pellets. The virus pellets were
571 resuspended in cold DMEM for storage at -80°C for transduction of cells.

572

573 *Generation of stable cell line*

574 To generate a Vero E6 cell line stably expressing Sec61β-GFP, $2x10^5$ Vero E6 cells were seeded in
575 one well of a 6-well plate and infected with one quarter of concentrated lentivirus expressing pLV-
576 ER-GFP produced from one 10-cm dish of HEK293T cells while seeding. After two days incubation,
577 monoclonal cells expressing GFP were sorted out using a SONY SH800S sorter. These transduced
578 cells were only used for ER imaging; all other experiments used wild type (WT) cells.

579

580 *SARS-CoV-2 viral stocks preparation*

581 The SARS-CoV-2 WA 1, isolate USA-WA1/2020 (NR-52281, BEI Resources) was passaged 3 times
582 in Vero E6-TMPRSS2 cells as previously described[60,61]. Briefly, a Vero E6-TMPRSS2 monolayer was
583 infected with virus obtained from BEI; post 72 hours of infection (hpi), P1 virus-containing tissue
584 culture supernatants were collected and stored at -80°C. Following titration, P1 virus stock was
585 used to generate a P2 stock by infecting Vero E6 TMPRSS2 monolayers with multiplicity of

586 infection (MOI) of 0.0001 for 72 hours. P2 virus was passaged again in Vero E6-TMPRSS2 cells to
587 obtain P3 stock. Viral titers were determined by standard plaque assay on Vero E6 cells.

588

589 *Infection of cells by SARS-CoV-2*

590 Vero E6 cells previously cultured in 8-well µ-slides were infected in the BSL-3 facility with SARS-
591 CoV-2 WA 1 (USA212 WA1/2020) in triplicates (MOI=0.5 SARS-CoV-2 WA1 (P3)) at an MOI of 2 for
592 6 hpi and MOI of 0.2 for 24 hpi. After 6 and 24 hrs of incubation, cells were washed with PBS and
593 fixed by 4% PFA (Electron Microscopy Sciences #15710) and 0.1% glutaraldehyde (Electron
594 Microscopy Sciences #16350) in PBS for 1 hour and removed from BSL-3 for further processing.
595 All work involving viral stock preparation and infection using WT SARS-CoV-2 was conducted at
596 the high containment BSL-3 facility of Stanford University according to CDC and institutional
597 guidelines. All the experiments were performed using a P3 SARS-CoV-2 USA-WA1/2020,
598 containing 100% WT population with no deletion in the spike multi-basic cleavage site.

599

600 *Synthesis of the RNA FISH probes*

601 vgRNA FISH probes targeting the ORF1a region of SARS-CoV-2[26] were ordered with 5AmMC6
602 modifications from Integrated DNA Technologies, Inc. in plate format of 25 nmol scale with
603 standard desalting. Each probe was dissolved in water to a final concentration of 100 µM. The
604 same set of probes was combined with equal volumes of each probe to get a stock of 100 µM
605 mixed probes. The mixed probes were further desalted using ethanol precipitation. Briefly, 120
606 µL 100 µM probes were mixed with 12 µL 3 M sodium acetate (pH 5.5), followed by 400 µL
607 ethanol. After precipitation at -80C overnight, probes were pelleted through centrifugation at
608 12,000x g for 10 min at 4°C, washed with precooled 70% (vol./vol.) ethanol three times, air dried,
609 and dissolved in water to make a 100 µM solution of probes. Then, 18 µL 100 µM probes were
610 mixed with 2 µL 1 M $NaHCO_3$ (pH 8.5), followed by 100 µg Alexa Fluor™ 647 succinimidyl ester
611 (NHS) (Invitrogen, A37573) or CF568 succinimidyl ester (NHS) (Biotium, 92131) dissolved in 2 µL
612 dry DMSO (Invitrogen, D12345). The mixture was incubated for 3 days at 37C in the dark for

613 conjugation and purified for 3 rounds using Monarch PCR & DNA Cleanup Kit (5 µg) (NEB, T1030S)
614 following the manufacturer's instructions. The estimated labeling efficiency of probes was
615 calculated using the following equation:

616 $$Modification\ ratio = \frac{20}{(A_{base} \times \varepsilon_{dye})\ /\ (A_{dye} \times \varepsilon_{base})}$$

617 where ε_{dye} is 239,000 $cm^{-1}M^{-1}$, ε_{base} is 8,919 $cm^{-1}M^{-1}$, A_{base} is the absorbance of the nucleic acid at
618 260 nm, and A_{dye} is the absorbance of the dye at 650 nm. For the probes labeled with CF568, ε_{dye}
619 is 100,000 $cm^{-1}M^{-1}$, ε_{base} is 8,919 $cm^{-1}M^{-1}$, A_{base} is the absorbance of the nucleic acid at 260 nm,
620 and A_{dye} is the absorbance of the dye at 562 nm.

621

622 *RNA FISH, immunofluorescence (IF), and CellMask staining*

623 Fixed cells from BLS3 as described above were washed twice with a freshly prepared 0.1% $NaBH_4$
624 solution at room temperature for 5 min, and washed with PBS three times. For staining without
625 CellMask (Thermo Fisher, C10046), cells were permeabilized in 70% ethanol at 4°C overnight. For
626 CellMask staining, cells were permeabilized in 0.1% Triton X-100 at room temperature for 30 min.

627 For RNA FISH staining, permeabilized cells were washed with 200 µL Wash Buffer A [40 µL Stellaris
628 RNA FISH Wash Buffer A (LGC Biosearch Technologies, SMF-WA1-60), 20 µL deionized formamide,
629 140 µL H2O] at room temperature for 5 min, and incubated with 110 µL Hybridization Buffer [99
630 µL Stellaris RNA FISH Hybridization Buffer (LGC Biosearch Technologies, SMF-HB1-10), 11 µL
631 deionized formamide] containing 1.1 µL 12.5 µM vgRNA FISH probes for 4 hours at 37°C in the
632 dark. Then cells were washed with Wash Buffer A for 30 min at 37°C in the dark, washed with
633 Wash Buffer A containing DAPI for 30 min at 37°C in the dark, and stored in Wash Buffer B (LGC
634 Biosearch Technologies, SMF-WB1-20) for imaging. DAPI was only added to the samples for
635 confocal imaging and not added to the samples for SR imaging.

636 For IF staining with antibodies, permeabilized cells were washed with PBS twice, incubated with
637 3% BSA in PBS at room temperature for 30 min, and incubated with primary antibodies in PBS at
638 37°C for 1 hour. After incubation with primary antibodies, cells were washed twice with PBST

639 buffer (0.1% Tween-20 in PBS) at room temperature for 5 min, washed with PBS once, incubated
640 with secondary antibodies in PBS at room temperature for 30 min, washed with PBST buffer three
641 times at room temperature for 5 min, and stored in PBS for imaging.

642 For simultaneous RNA FISH and IF staining, permeabilized cells were washed with 200 µL Wash
643 Buffer A at room temperature for 5 min, and incubated with 110 µL Hybridization Buffer (99 µL
644 Stellaris RNA FISH Hybridization Buffer, 11 µL deionized formamide) containing 1.1 µL 12.5 µM
645 vgRNA FISH probes, 1 U/µL RNase inhibitor (NxGen, F83923-1), and primary antibodies for 4 hours
646 at 37°C in the dark. Then cells were washed with 2xSSC buffer once, washed with Wash Buffer A
647 containing secondary antibodies for 30 min at 37°C in the dark, washed with Wash Buffer A for
648 30 min at 37°C in the dark, washed with Wash Buffer B once, and stored in Wash Buffer B for
649 imaging. For CellMask staining, several more steps were performed from here. Cells were washed
650 with PBS once, stained with 1:20k CellMask and 1 U/µL RNase inhibitor in PBS for 20 min at room
651 temperature in the dark, and washed with PBS three times before imaging.

652

653 *RNA FISH and IF staining of purified virions*

654 8-well µ-slides (ibidi, 80827-90) were first treated with poly-D-lysine solution (Thermo Fisher,
655 A3890401) at 4°C overnight. Then in the BSL-3 facility, the poly-D-lysine solution was removed
656 and 150 µL SARS-CoV-2 WA1 (P3) virus solution of titer 1.82×10^5 PFU/mL was added into one well
657 of poly-D-lysine-treated 8-well µ-slides for incubation at 4°C for 24 hours to coat the virions onto
658 the surface of the well. After incubation, the medium containing virions was removed and the
659 well was washed with PBS twice. Virions on the surface of the well were fixed with 4% PFA in PBS
660 for 1 hour at room temperature and the sample was removed from BSL-3. The sample was
661 washed twice with a freshly prepared 0.1% $NaBH_4$ solution at room temperature for 5 min, and
662 then washed with PBS three times. The fixed virions were permeabilized in 70% ethanol at 4°C
663 overnight and washed with PBS twice. For the group with Proteinase K digestion, virions were
664 incubated with 0.2 mg/mL Proteinase K (NEB #P8107S) in 120 µL PBS at 37°C for 30 min and
665 washed with PBST buffer three times. Virions were washed with Wash Buffer A once and
666 incubated with 110 µL Hybridization Buffer (99 µL Stellaris RNA FISH Hybridization Buffer, 11 µL

667 deionized formamide) containing 1.1 µL 12.5 µM vgRNA FISH probes, 1 U/µL RNase inhibitor, and
668 primary antibodies for 4 hours at 37°C in the dark. Then virions were washed with 2xSSC buffer
669 once, washed with Wash Buffer A containing secondary antibodies for 30 min at 37°C in the dark,
670 washed with Wash Buffer A for 30 min at 37°C in the dark, washed with Wash Buffer B once, and
671 stored in Wash Buffer B for imaging.

672

673 *Labeling of newly replicated RNA with BrUTP*

674 Vero E6 cells cultured in 8-well µ-slides were infected with SARS-CoV-2 WA 1 (USA212 WA1/2020)
675 as described above. After 24 hours of incubation, the culture medium was switched to low
676 glucose DMEM medium (Thermo Fisher, 10567014) supplemented with 20 mM glucosamine for
677 30 mins to deplete uridine. Both infected and uninfected groups were further treated with 15 µM
678 actinomycin D (Sigma, A4262) at 37°C for 30 min to inhibit cellular transcription. To transfect cells
679 with BrUTP, each well of cells was treated with 10 mM BrUTP (Sigma, B7166) and 12 µL
680 Lipofectamine 2000 (Thermo Fisher, 11668030) for 1 hour at 37°C. Cells were then washed twice
681 with PBS, followed by 4% PFA and 0.1% glutaraldehyde fixation for 1 hour, and removed from BSL-
682 3 following BSL-3 SOP of sample removal. The fixed cells were then washed twice with a freshly
683 prepared 0.1% $NaBH_4$ solution at room temperature for 5 min, washed with PBS three times,
684 permeabilized in 70% ethanol at 4°C overnight, and washed twice with PBS.

685 The co-staining of BrU and nsp12 with antibodies follows the IF staining procedure detailed in the
686 section "RNA FISH, immunofluorescence (IF), and CellMask staining". For the co-staining of BrU
687 and vgRNA, cells were first incubated with BrU antibody and 1 U/µL RNase inhibitor in PBS at 37°C
688 for 30 min. Cells were then washed twice with PBST buffer, washed once with PBS, and incubated
689 with the secondary antibody and 0.5 U/µL RNase inhibitor in PBS at room temperature for 30
690 min. Cells were then washed with PBST buffer three times, fixed again with 4% PFA and 0.1%
691 glutaraldehyde in PBS at room temperature for 10 min, and washed with PBS three times. After
692 that, cells were washed with Wash Buffer A at room temperature for 5 min, incubated with 110
693 µL Hybridization Buffer containing 1.1 µL 12.5 µM vgRNA FISH probes and 1 U/µL RNase inhibitor

694 for 4 hours at 37°C in the dark. Then cells were washed twice with Wash Buffer A for 30 min at
695 37°C in the dark and stored in Wash Buffer B for imaging.

696

697 *Spinning disk confocal microscopy*

698 Confocal microscopy was performed at the Stanford University Cell Sciences Imaging Core Facility
699 with a Nikon TiE inverted spinning disk confocal microscope (SDCM) equipped with a
700 Photometrics Prime 95B camera, a CSU-X1 confocal scanner unit with microlenses, and 405 nm,
701 488 nm, 561 nm, and 642 nm lasers, using the 60x/1.27 NA PLAN APO IR water immersion
702 objective. Images were taken using NIS Elements software version 4.60 with Z stacks at 0.3 µm
703 steps. The camera pixel size of SDCM is 0.183 µm/pixel and the pinhole size is 50 µm. Only one Z
704 slice is used for all images shown.

705

706 *Analysis of confocal data*

707 To extract the intensity of vgRNA, dsRNA and RdRp in each infected cell (Fig. S2c, e-h), the
708 summation projection of each z stack was created by Fiji[62]. The intensity of each target species in
709 each cell was measured by Fiji, subtracting the background of the same color channel. The
710 infected cells were characterized manually into three types based on the morphology of vgRNA.
711 Type 1 shows scattered dot-like localization of vgRNA. Type 3 shows large clustered vgRNA. Type
712 2 contains features of both type 1 and type 3.

713

714 *Optimization of antibody concentrations*

715 We optimized the concentration of antibodies in this study by quantifying their signal-to-
716 background ratio (SBR), where the signal is the brightness of the IF labeling in the cells that
717 express the given target (virus-infected sample or cells expressing Sec61β-GFP), and the
718 background is the brightness in the negative control cells (not-infected or WT cells).

To optimize the concentration of primary antibodies against the viral targets, different concentrations of the primary antibody were applied to stain Vero E6 cells in SARS-CoV-2-infected and not-infected samples under a constant secondary antibody concentration (Fig. S19). To optimize the concentration of secondary antibodies, different concentrations of the secondary antibody were applied to stain Vero E6 cells in infected (virus+) and not-infected (virus−) samples under a constant primary antibody concentration (Fig. S20). For each cell, a 11 pixel x 11 pixel box was drawn in the region with brightest signal in the cell and the mean intensity within that region was measured to represent the intensity of target antibody in that cell. The SBR was calculated, after subtraction of the dark signal I_{dark}, using the following equation:

$$SBR = \frac{< I_{virus+} - I_{dark} >}{< I_{virus-} - I_{dark} >}$$

To optimize the concentration of the anti-GFP antibodies, different concentrations of primary antibody were applied to stain Vero E6 Sec61B-GFP cells and WT Vero E6 cells under a constant secondary antibody concentration (Fig. S19). For each cell, a 11 pixel x 11 pixel box was drawn in the region with the brightest signal in the cell and the mean intensities of both the GFP and the antibody signals within that region were measured after subtraction of the dark signals. To account for the variable expression levels among different cells, the IF signal I_{IF} was normalized by the GFP signal I_{GFP} within the given region. The SBR was calculated using the following equation:

$$SBR = \frac{< I_{IF,Sec61B\text{-}GFP}/I_{GFP,Sec61B\text{-}GFP} >}{< I_{IF,WT}/I_{GFP,WT} >}$$

For the primary antibodies against GFP, nsp3, nucleocapsid, nsp12 and for the secondary antibody for the dsRNA labeling, we chose the antibody concentration that produces the highest SBR as the optimal concentration. For the primary antibodies against spike S2 and dsRNA and for the secondary antibody for the spike S2 labeling, we chose the concentration that yields the second highest SBR because it provides a significantly lower non-specific background with only a minor decrease of the estimated SBR.

745

746 *Optical setup for SR microscopy*

747 (d)STORM SR microscopy was performed on a custom-built system (Fig. S14), consisting of a Nikon
748 Diaphot 200 inverted microscope frame with an oil-immersion objective 60x/1.35 NA (Olympus
749 UPLSAPO60XO) and a Si EMCCD camera (Andor iXon Ultra 897). We used 642 nm and 560 nm 1W
750 continuous-wave (CW) lasers (MPB Communications Inc.) for excitation of AF647 or CellMask and
751 CF568 or CF583R, accordingly. For reactivation of fluorophores from the dark state we used a 405
752 nm 50 mW CW diode laser (Coherent OBIS). All laser beams were expanded and co-aligned in
753 free space and coupled into a square-core multi-mode fiber with a shaker for speckle reduction
754 (Newport F-DS-ASQR200-FC/PC). The output tip of the fiber (200 x 200 μm^2 core size) was imaged
755 with a 10x/0.25 NA objective and magnified to achieve a square illumination region of 47.6 x 47.6
756 μm^2 with a constant intensity in the sample image plane of the main objective. The fluorescence
757 was split from the excitation light with a multi-band dichroic mirror (ZT405/488/561/640rpcv2,
758 Chroma) and filtered with dichroic filters (ZET635NF, ZET561NF, T690LPxxr, all Chroma). The
759 fluorescence of AF647 and CellMask was additionally filtered with a band-pass filter (ET685/70M,
760 Chroma) and that of CF568 and CF583R with a combination of 561LP and 607/70BP (Semrock,
761 EdgeBasic and BrightLine). The sample image was focused with a tube lens (f = 400 mm) on the
762 EMCCD camera, providing a pixel size of 117 x 117 nm^2 in sample coordinates.

763 Axial drift was compensated with a custom Focus Lock system[63]. We used an 808 nm fiber-coupled
764 diode laser (Thorlabs S1FC808) whose output fiber tip was conjugated with the back focal plane
765 of the imaging objective, allowing changing the angle of this beam out of the objective by
766 translating the fiber tip (Fig. S14). This inclined beam was partially reflected from the coverslip-
767 water interface and the reflected beam was focused with a cylindrical lens onto a CMOS sensor
768 (UI-3240CP-NIR, IDS Imaging). The 808 nm beam was aligned such that the image of the reflected
769 beam would shift laterally when the axial position of the sample changes. The sample was
770 mounted on two stacked piezo stages (U-780.DOS for coarse and P-545.3C8S for fine movement,
771 both Physik Instrumente). The position of the reflected beam image was recorded when the
772 sample was set at the desired Z position for imaging. During imaging, the Z-position of the fine

773 stage was directed to move proportionally to the shift of the reflected beam image from the
774 recorded position, compensating for Z-drift. The Focus Lock control code was programmed in
775 Matlab (MathWorks, Inc.).

776

777 *SR imaging procedure*

778 For (d)STORM, the sample chamber was filled with 300 µl of a photoblinking buffer consisting of
779 200 U/ml glucose oxidase, 1000 U/ml catalase, 10% w/v glucose, 200 mM Tris-HCl pH 8.0, 15 mM
780 NaCl and 50 mM cysteamine. The buffer was prepared using the following stock solutions[48]: 1)
781 4 kU/ml glucose oxidase (G2133, Sigma), 20 kU/ml catalase (C1345, Sigma), 25 mM KCl (P217,
782 Fisher), 4 mM TCEP (646547, Sigma), 50% v/v glycerol (BP229, Fisher) and 22 mM Tris-HCl pH 7.0
783 (BP1756, Fisher), stored at −20 °C; 2) 1 M cysteamine-HCl (30080, Sigma), stored at −20 °C; 3) 37%
784 w/v glucose (49139, Sigma) with 56 mM NaCl (S271, Fisher) and 0.74 M Tris-HCl pH 8.0
785 (J22638.AE, Fisher), stored at +4 °C. For samples with RNA FISH labeling, the buffer was
786 supplemented with 1 U/µl of an RNase inhibitor (302811, LGC Biosearch Technologies).

787 The SR imaging started with a DL image of cells from each fluorophore at a low power (*e.g.*, 2
788 W/cm^2). For (d)STORM acquisitions, we began with AF647 or CellMask, followed by CF568 or
789 CF583R[64]. We used an excitation power density of ~20 kW/cm^2 for shelving and blinking of CF568,
790 ~13 kW/cm^2 for CF583R and 6-20 kW/cm^2 for AF647. The power density of the 405 nm
791 illumination for both dyes was increased from 0 to 50 W/cm^2 throughout an acquisition to keep
792 the reactivation rate approximately constant. The exposure time was 10.57 ms per frame and the
793 calibrated EM gain was either 43 or 84. The image recording started after the initial shelving phase
794 upon observation of clear SM blinking; the blinking movies were acquired for approximately
795 $6 \cdot 10^4 – 8 \cdot 10^4$ frames for each fluorophore.

796

797 *SR data analysis*

798 SM movies were processed with the ThunderStorm plugin[65] for Fiji. First, the images were filtered
799 with a wavelet filter with a b-spline order of 3 and a scale of 2. The coarse localizations were

found as local maxima with an 8-neighborhood connectivity and a threshold of 2·std(Wave.F1). These localizations were weighted least squares-fitted with the integrated Gaussian model using a radius of 4 pixels and an initial sigma of 1.1. Then, we performed drift correction estimated by cross-correlation between successive subsets of localizations in ThunderStorm, or in SharpViSu[66] when the drift correction in ThunderStorm was unsuccessful. For further processing, we kept only localizations with fitted sigma between 160 nm and 80 nm. This choice effectively rejects molecules away from the focal plane, providing an approximate axial sectioning of the images to roughly 500 nm[67].

For image registration, we imaged 200 nm TetraSpeck beads (T7280, Thermo Fisher Scientific) in both channels, whose images were processed similarly to the SM movies. The transformation between the channels was calculated using an affine transformation with help of Matlab function 'fitgeotrans'. The calculated transformation was then applied to the CF568 or CF583R localizations using a Matlab function 'transformPointsInverse'.

Localizations found within 50 nm on consecutive frames that could originate from multiple localizations of a single molecule were treated in two ways. For SR images, to improve the resolution, these localizations were refined by selecting them from a normal distribution with a mean at the weighted mean of the initial localizations and a standard deviation (SD) that equals $120 \cdot (N_{ph})^{-1/2}$ nm, where N_{ph} is the total number of photons acquired from all localizations in the given consecutive series[48]. For data analysis other than SR image reconstruction, to suppress overcounting, the localizations of the consecutive series were reduced to a single localization at the weighted mean position. The weights of localizations were proportional to the photon counts of these individual localizations. After this correction, the SR data of antibody-detected Spike, N, nsp12, BrU, nsp8, nsp7 was additionally filtered by removing localizations that had 3 or less neighbors within 30 nm. SR images were reconstructed as 2D histograms with a bin size of 20 x 20 nm^2. However, SR images where one of the channels contained the CellMask labeling had a bin size of 30 x 30 nm^2. SR images acquired with CellMask were additionally filtered with a Gaussian filter with $\sigma = 0.5$ pixels.

Cluster analysis with BIC-GMM

Gaussian Mixture Models (GMM) implemented in Python were fitted to vgRNA and dsRNA localization datasets, yielding a representation of localization densities as a collection of potentially elliptical and/or rotated 2D Gaussians. The number of components most suitable for each field of view was determined using an iterative grid search, evaluating 4 candidate GMMs using the Bayesian Information Criterion (BIC)[68]. The first grid iteration tested [1, 2500] components with test points $t_i = \{1, 834, 1667, 2500\}$, where i denotes the index in the set such that $t_0 = 1$. For each iteration of the grid search, the model with the lowest BIC (corresponding to the best candidate), t_k was selected, and the next iteration of the grid was narrowed, to be bounded by $[t_{max\,(k-1,\,0)} + 1,\ t_{min\,(k+1,\,3)} - 1]$, until the stride of the grid was 1 component, or the test point with the best BIC was on a rail (k = 0 or 3). To reduce memory requirements, this GMM optimization was performed on a random subset of up to 200,000 localizations from each data set, but the optimized GMM was then used to predict a component assignment for all original localizations. These components were regarded as clusters, and refined by removing localizations with a log probability of being an event from their assigned Gaussian component of less than −25. The radius of gyration, Rg, was then calculated for each cluster, and the number of localizations in each cluster, N_{loc}, was used to approximate a cluster density as $\delta = N_{loc} / (\pi \cdot Rg^2)$. Clusters with δ below a threshold of 0.008 localizations/nm^2 for dsDNA, or below an ROI-dependent threshold between 0.005 and 0.013 localizations/nm^2 for vgRNA, were removed from further quantification as sparse background. This analysis and resulting visualizations were carried out in the PYthon Microscopy Environment (https://doi.org/10.5281/zenodo.4289803)[69], using a plugin (github.com/barentine/bic-gmm) and the scikit-learn GMM implementation[70].

Counting of vgRNA molecules in the clusters

The number of vgRNA molecules in a vgRNA cluster was defined as a quotient between the number of vgRNA-FISH localizations in the cluster and the average number of localizations produced by a single FISH-labeled vgRNA molecule in the given cell. The average number of

855 localizations per vgRNA molecule was estimated from isolated nanoscale vgRNA puncta in the
856 cytoplasm (Fig. 3a). This number was defined as the median of the number of localizations within
857 50 nm from each localization in the region with vgRNA puncta. The estimated number of vgRNA
858 molecules was calculated for every cluster determined by the BIC-GMM cluster analysis and the
859 median value per cell was shown in a chart (Fig. 3b-c).

860

861 *Counting of nsp12 puncta in the vgRNA clusters*

862 The center of nsp12 puncta is obtained by fitting the SR images in ThunderStorm[65]. The SR
863 localizations of nsp12 were first converted into a 2D histogram image with a bin size of
864 20 x 20 nm^2. The approximate localization of the center was found as a centroid of connected
865 components with a threshold of 5·std(Wave.F1) without filter. These localizations were least
866 squares-fitted with the integrated Gaussian model using a fitting radius of 2 pixels and an initial
867 sigma of 0.4. We next removed duplicates among localizations within a 20 nm radius. The puncta
868 whose sigma were smaller than 5 nm were further filtered out to avoid localizing single-pixel-
869 sized background localizations. For each vgRNA cluster with its center and the radius of gyration
870 (Rg) determined using BIC-GMM, we counted the number of nsp12 puncta within a 1.5·Rg
871 distance of the center of the vgRNA cluster. For nsp12 puncta found within the cutoff distance of
872 more than one vgRNA cluster, we assigned them to their closest cluster based on the relative
873 distance d/Rg, with d being the distance between the center of the vgRNA cluster and center of
874 the nsp12 punctum.

875

876 *Bivariate pair-correlation functions*

877 For calculation of bivariate pair-correlation functions[29] $g_{12}(r)$, we first manually selected the
878 cytoplasmic regions with dense vgRNA clusters. The pair-correlation functions were calculated by
879 counting the number of localizations of the second species within a distance between r and r+dr
880 from each localization of the first species. These were normalized by dividing the number of
881 localizations by the area of the corresponding ring of radii r and r+dr and by the average density

882 of the second species in the region. Finally, the obtained numbers were averaged across the
883 localizations of the first species. r was scanned over the range between 0 and 500 nm and dr was
884 set to 1 nm. For the complete spatial randomness (CSR) case, a test CSR dataset was generated
885 with the same average density as for the experimental case across the same ROI. $g_{12}(r)$ traces
886 were calculated from these CSR datasets as described above. No edge effect correction was
887 performed leading to a slight decrease of $g_{12}(r)$ at large r. Plots in the figures display experimental
888 and CSR $g_{12}(r)$ for each analyzed cell as faint lines as well as the mean $g_{12}(r)$ calculated from all
889 cells in bold lines.

890

891 *Estimation of RNA FISH labeling efficiency in virions*

892 Dye molecules inside virions were counted using fluorescence bleaching with SM calibration.
893 Virions attached to the coverslip were labeled using the RNA-FISH+IF protocol with PFA-only
894 fixation. The density of virions was around 0.5 μm^{-2} ensuring observation of most virions as single
895 DL spots without overlap (Fig. S1a, d). vgRNA was FISH-labeled with AF647 and spike protein was
896 IF-stained with CF568. Glass-bottom chambers with virions were kept in PBS for this experiment.
897 Samples were illuminated with 642 nm light at 20 W/cm^2 and were imaged with an exposure time
898 of 200 ms and an EM gain of 43 until bleaching of all AF647 in the imaging region (around 200 s).
899 A separate DL image of spike was taken with 560 nm excitation. The AF647 bleaching movies were
900 processed in ThunderStorm using a wavelet filter with a b-spline order of 3 and a scale of 2, a
901 local maximum approximate localization with a threshold of 1.2·std(Wave.F1) and an 8-
902 neighborhood connectivity. These localizations were weighted least squares-fitted with the
903 integrated Gaussian model using a radius of 3 pixels and an initial sigma of 1.1. Then, we kept
904 only localizations with sigma < 160 nm & sigma > 80 nm and removed duplicates within 300 nm
905 on each frame.

906 Further processing was done in Matlab with a custom script. We considered only vgRNA-AF647
907 localizations that had a spike-CF568 signal within 200 nm to avoid counting AF647 molecules
908 outside virions. The bleaching time traces (Fig. S1c, f) were found by searching in consecutive
909 frames within 200 nm of the localization from the first frame and allowing up to 5 empty frames

910 between frames with detections. The number of bleaching steps was defined as the rounded
911 quotient between the initial and the final brightness of a spot in a time trace serving as the SM
912 calibration. For each bleaching trace, the initial brightness (in photons) was defined as the median
913 value of the brightness in the first 4 localizations and the final brightness as the median brightness
914 value of the last 4 localizations. If the trace contained only 7-8 detections, the range for the initial
915 and the final brightness was reduced to 3 frames; for traces with 5-6 detections, this was reduced
916 to 2; for traces with 3-4 frames – to 1; for traces containing only 1 or 2 detections, the number of
917 bleaching steps was set to 1. For each analyzed region containing around 200 bleaching traces,
918 the number of bleaching steps was fitted with a zero-truncated Poisson distribution (Fig. S1g-h).
919 The expected values ± SD obtained from the fit of 5 regions for each of not-treated and PK-treated
920 cells are shown in a chart (Fig. S1i).

921

922 **Data availability**

923 Source data for analysis figures are provided with this paper. The code utilized in this study is
924 available at Stanford Digital Repository at https://doi.org/10.25740/td954gx5320. All data
925 generated in this study are available from the Corresponding Authors upon reasonable request.

926

927 **Author contribution**

928 L.A., M.H., L.S.Q. and W.E.M. conceived the project. L.A. designed the optical set-up, performed
929 the SR acquisitions and data analysis. M.H. performed cell culture, labeling and confocal imaging.
930 Y.Z. performed confocal and SR data analysis and helped with sample preparation and confocal
931 imaging. J.G. and P.P. performed SARS-CoV-2 infection experiments at the BSL-3 facility with staff
932 listed in the Acknowledgements. A.R.R. contributed to the concept and SR experiments at the
933 early stages of the project. A.E.S.B. designed the BIC-GMM cluster analysis method and
934 contributed to the optical set-up design. A.B. performed portions of the BrU SR imaging. L.A. and
935 W.E.M. wrote the manuscript with input from all authors.

936

Acknowledgements

We thank Amol Pohane for assistance with the cell culturing in the BSL-3 facility. We thank Leiping Zeng for sample preparation and discussion about the results and experimental plan with the other authors. This work was supported in part by the National Institute of General Medical Sciences Grant Nos. R35GM118067 (to W.E.M.) and the National Institutes of Health Common Fund 4D Nucleome Program No. U01 DK127405 (to L.S.Q.). We also acknowledge Stanford University Cell Sciences Imaging Core Facility (RRID:SCR_017787). L.S.Q. is a Chan Zuckerberg Biohub – San Francisco Investigator, and W.E.M. is a Sarafan ChEM-H Fellow.

An earlier version of this research was published on bioRxiv on November 8, 2023 https://doi.org/10.1101/2023.11.07.566110

References

1. Schmidt N*, et al.* The SARS-CoV-2 RNA–protein interactome in infected human cells. *Nature Microbiology* **6**, 339-353 (2021).

2. Flynn RA*, et al.* Discovery and functional interrogation of SARS-CoV-2 RNA-host protein interactions. *Cell* **184**, 2394-2411.e2316 (2021).

3. Knoops K*, et al.* SARS-coronavirus replication is supported by a reticulovesicular network of modified endoplasmic reticulum. *PLoS Biol* **6**, e226 (2008).

4. Snijder EJ*, et al.* A unifying structural and functional model of the coronavirus replication organelle: Tracking down RNA synthesis. *PLoS Biol* **18**, e3000715 (2020).

5. Klein S*, et al.* SARS-CoV-2 structure and replication characterized by in situ cryo-electron tomography. *Nat Commun* **11**, 5885 (2020).

6. Betzig E*, et al.* Imaging intracellular fluorescent proteins at nanometer resolution. *Science* **313**, 1642-1645 (2006).

7. Rust MJ, Bates M, Zhuang X. Sub-diffraction-limit imaging by stochastic optical reconstruction microscopy (STORM). *Nat Methods* **3**, 793-796 (2006).

8. Heilemann M*, et al.* Subdiffraction-Resolution Fluorescence Imaging with Conventional Fluorescent Probes. *Angew Chem Int Ed* **47**, 6172-6176 (2008).

9. Klar TA, Jakobs S, Dyba M, Egner A, Hell SW. Fluorescence microscopy with diffraction resolution barrier broken by stimulated emission. *Proceedings of the National Academy of Sciences of the United States of America* **97**, 8206-8210 (2000).

10. Gustafsson MGL. Surpassing the lateral resolution limit by a factor of two using structured illumination microscopy. *J Microsc* **198**, 82-87 (2000).

11. Xu K, Zhong G, Zhuang X. Actin, Spectrin, and Associated Proteins Form a Periodic Cytoskeletal Structure in Axons. *Science* **339**, 452-456 (2013).

12. Andronov L, Ouararhni K, Stoll I, Klaholz BP, Hamiche A. CENP-A nucleosome clusters form rosette-like structures around HJURP during G1. *Nature Communications* **10**, 4436 (2019).

13. Reinhardt SCM*, et al.* Ångström-resolution fluorescence microscopy. *Nature* **617**, 711-716 (2023).

14. Baddeley D, Bewersdorf J. Biological Insight from Super-Resolution Microscopy: What We Can Learn from Localization-Based Images. *Annual Review of Biochemistry* **87**, 965-989 (2018).

15. Wang J*, et al.* Multi-color super-resolution imaging to study human coronavirus RNA during cellular infection. *Cell Reports Methods* **2**, 100170 (2022).

16. Jackson CB, Farzan M, Chen B, Choe H. Mechanisms of SARS-CoV-2 entry into cells. *Nature Reviews Molecular Cell Biology* **23**, 3-20 (2022).

17. Timothy Ting-Hsuan W*, et al.* Activated interstitial macrophages are a predominant target of viral takeover and focus of inflammation in COVID-19 initiation in human lung. *bioRxiv*, 2022.2005.2010.491266 (2023).

1004
1005 18. Hillen HS, Kokic G, Farnung L, Dienemann C, Tegunov D, Cramer P. Structure of replicating
1006 SARS-CoV-2 polymerase. *Nature* **584**, 154-156 (2020).

1007
1008 19. Park GJ*, et al.* The mechanism of RNA capping by SARS-CoV-2. *Nature* **609**, 793-800 (2022).

1009
1010 20. Decroly E, Ferron F, Lescar J, Canard B. Conventional and unconventional mechanisms for
1011 capping viral mRNA. *Nature Reviews Microbiology* **10**, 51-65 (2012).

1012
1013 21. Zimmermann L*, et al.* SARS-CoV-2 nsp3 and nsp4 are minimal constituents of a pore
1014 spanning replication organelle. *Nature Communications* **14**, 7894 (2023).

1015
1016 22. Eymieux S*, et al.* Ultrastructural modifications induced by SARS-CoV-2 in Vero cells: a
1017 kinetic analysis of viral factory formation, viral particle morphogenesis and virion release.
1018 *Cellular and Molecular Life Sciences* **78**, 3565-3576 (2021).

1019
1020 23. Doyle N, Simpson J, Hawes PC, Maier HJ. Coronavirus RNA Synthesis Takes Place within
1021 Membrane-Bound Sites. *Viruses* **13**, 2540 (2021).

1022
1023 24. V'Kovski P, Kratzel A, Steiner S, Stalder H, Thiel V. Coronavirus biology and replication:
1024 implications for SARS-CoV-2. *Nat Rev Microbiol* **19**, 155-170 (2021).

1025
1026 25. Wolff G*, et al.* A molecular pore spans the double membrane of the coronavirus replication
1027 organelle. *Science* **369**, 1395-1398 (2020).

1028
1029 26. Lee JY*, et al.* Absolute quantitation of individual SARS-CoV-2 RNA molecules provides a
1030 new paradigm for infection dynamics and variant differences. *eLife* **11**, e74153 (2022).

1031
1032 27. Pepe A, Pietropaoli S, Vos M, Barba-Spaeth G, Zurzolo C. Tunneling nanotubes provide a
1033 route for SARS-CoV-2 spreading. *Science Advances* **8**, eabo0171 (2022).

1034
1035 28. Sherman E*, et al.* Functional Nanoscale Organization of Signaling Molecules Downstream
1036 of the T Cell Antigen Receptor. *Immunity* **35**, 705-720 (2011).

1037
1038 29. Razvag Y, Neve-Oz Y, Sajman J, Reches M, Sherman E. Nanoscale kinetic segregation of TCR
1039 and CD45 in engaged microvilli facilitates early T cell activation. *Nature Communications*
1040 **9**, 732 (2018).

30. Sawicki SG, Sawicki DL. Coronavirus minus-strand RNA synthesis and effect of cycloheximide on coronavirus RNA synthesis. *Journal of Virology* **57**, 328-334 (1986).

31. Gao Y*, et al.* Structure of the RNA-dependent RNA polymerase from COVID-19 virus. *Science* **368**, 779-782 (2020).

32. Ahn D-G, Choi J-K, Taylor DR, Oh J-W. Biochemical characterization of a recombinant SARS coronavirus nsp12 RNA-dependent RNA polymerase capable of copying viral RNA templates. *Archives of Virology* **157**, 2095-2104 (2012).

33. Naydenova K*, et al.* Structure of the SARS-CoV-2 RNA-dependent RNA polymerase in the presence of favipiravir-RTP. *Proceedings of the National Academy of Sciences* **118**, e2021946118 (2021).

34. Gosert R, Kanjanahaluethai A, Egger D, Bienz K, Baker Susan C. RNA Replication of Mouse Hepatitis Virus Takes Place at Double-Membrane Vesicles. *Journal of Virology* **76**, 3697-3708 (2002).

35. Heinrich BS, Cureton DK, Rahmeh AA, Whelan SPJ. Protein Expression Redirects Vesicular Stomatitis Virus RNA Synthesis to Cytoplasmic Inclusions. *PLOS Pathogens* **6**, e1000958 (2010).

36. Cortese M*, et al.* Integrative Imaging Reveals SARS-CoV-2-Induced Reshaping of Subcellular Morphologies. *Cell Host & Microbe* **28**, 853-866.e855 (2020).

37. Lang S*, et al.* An Update on Sec61 Channel Functions, Mechanisms, and Related Diseases. *Front Physiol* **8**, 887 (2017).

38. Hsu JC-C, Laurent-Rolle M, Pawlak JB, Wilen CB, Cresswell P. Translational shutdown and evasion of the innate immune response by SARS-CoV-2 NSP14 protein. *Proceedings of the National Academy of Sciences* **118**, e2101161118 (2021).

39. Mönkemöller V, Schüttpelz M, McCourt P, Sørensen K, Smedsrød B, Huser T. Imaging fenestrations in liver sinusoidal endothelial cells by optical localization microscopy. *Physical Chemistry Chemical Physics* **16**, 12576-12581 (2014).

40. Oudshoorn D*, et al.* Expression and Cleavage of Middle East Respiratory Syndrome Coronavirus nsp3-4 Polyprotein Induce the Formation of Double-Membrane Vesicles That Mimic Those Associated with Coronaviral RNA Replication. *mBio* **8**, 10.1128/mbio.01658-01617 (2017).

41. Han Y-S*, et al.* Papain-Like Protease 2 (PLP2) from Severe Acute Respiratory Syndrome Coronavirus (SARS-CoV): Expression, Purification, Characterization, and Inhibition. *Biochemistry* **44**, 10349-10359 (2005).

42. Shin D*, et al.* Papain-like protease regulates SARS-CoV-2 viral spread and innate immunity. *Nature* **587**, 657-662 (2020).

43. Bai Z, Cao Y, Liu W, Li J. The SARS-CoV-2 Nucleocapsid Protein and Its Role in Viral Structure, Biological Functions, and a Potential Target for Drug or Vaccine Mitigation (2021).

44. Scherer KM*, et al.* SARS-CoV-2 nucleocapsid protein adheres to replication organelles before viral assembly at the Golgi/ERGIC and lysosome-mediated egress. *Science Advances* **8**, eabl4895 (2022).

45. Xia X. Domains and Functions of Spike Protein in SARS-Cov-2 in the Context of Vaccine Design (2021).

46. Hartenian E, Nandakumar D, Lari A, Ly M, Tucker JM, Glaunsinger BA. The molecular virology of coronaviruses. *J Biol Chem* **295**, 12910-12934 (2020).

47. Baggen J, Vanstreels E, Jansen S, Daelemans D. Cellular host factors for SARS-CoV-2 infection. *Nature Microbiology* **6**, 1219-1232 (2021).

48. Andronov L, Genthial R, Hentsch D, Klaholz BP. splitSMLM, a spectral demixing method for high-precision multi-color localization microscopy applied to nuclear pore complexes. *Communications Biology* **5**, 1100 (2022).

49. Storti B*, et al.* A spatial multi-scale fluorescence microscopy toolbox discloses entry checkpoints of SARS-CoV-2 variants in Vero E6 cells. *Computational and Structural Biotechnology Journal* **19**, 6140-6156 (2021).

50. Cao C*, et al.* The architecture of the SARS-CoV-2 RNA genome inside virion. *Nature Communications* **12**, 3917 (2021).

1116
1117 51. Lan TCT*, et al.* Secondary structural ensembles of the SARS-CoV-2 RNA genome in infected
1118 cells. *Nature Communications* **13**, 1128 (2022).

1119
1120 52. Gopal A, Zhou ZH, Knobler CM, Gelbart WM. Visualizing large RNA molecules in solution.
1121 *RNA* **18**, 284-299 (2012).

1122
1123 53. Schonborn J, Oberstrass J, Breyel E, Tittgen J, Schumacher J, Lukacs N. Monoclonal
1124 antibodies to double-stranded RNA as probes of RNA structure in crude nucleic acid
1125 extracts. *Nucleic Acids Res* **19**, 2993-3000 (1991).

1126
1127 54. Ku J*, et al.* Reactive Polymer Targeting dsRNA as Universal Virus Detection Platform with
1128 Enhanced Sensitivity. *Biomacromolecules* **21**, 2440-2454 (2020).

1129
1130 55. Deng J*, et al.* SARS-CoV-2 NSP8 suppresses type I and III IFN responses by modulating the
1131 RIG-I/MDA5, TRIF, and STING signaling pathways. *Journal of Medical Virology* **95**, e28680
1132 (2023).

1133
1134 56. Kumar P*, et al.* The nonstructural protein 8 (nsp8) of the SARS coronavirus interacts with
1135 its ORF6 accessory protein. *Virology* **366**, 293-303 (2007).

1136
1137 57. Snijder EJ*, et al.* Ultrastructure and origin of membrane vesicles associated with the severe
1138 acute respiratory syndrome coronavirus replication complex. *J Virol* **80**, 5927-5940 (2006).

1139
1140 58. Stertz S*, et al.* The intracellular sites of early replication and budding of SARS-coronavirus.
1141 *Virology* **361**, 304-315 (2007).

1142
1143 59. Ulasli M, Verheije MH, de Haan CAM, Reggiori F. Qualitative and quantitative
1144 ultrastructural analysis of the membrane rearrangements induced by coronavirus. *Cellular*
1145 *Microbiology* **12**, 844-861 (2010).

1146
1147 60. Chiem K, Ye C, Martinez-Sobrido L. Generation of Recombinant SARS-CoV-2 Using a
1148 Bacterial Artificial Chromosome. *Current Protocols in Microbiology* **59**, e126 (2020).

1149
1150 61. Ye C*, et al.* Rescue of SARS-CoV-2 from a Single Bacterial Artificial Chromosome. *mBio* **11**,
1151 10.1128/mbio.02168-02120 (2020).

1152

62. Schindelin J*, et al.* Fiji: an open-source platform for biological-image analysis. *Nature methods* **9**, 676-682 (2012).

63. Barentine AES*, et al.* An integrated platform for high-throughput nanoscopy. *Nature Biotechnology*, (2023).

64. Wang B, Xiong M, Susanto J, Li X, Leung W-Y, Xu K. Transforming Rhodamine Dyes for (d)STORM Super-Resolution Microscopy via 1,3-Disubstituted Imidazolium Substitution. *Angewandte Chemie International Edition* **61**, e202113612 (2022).

65. Ovesny M, Krizek P, Borkovec J, Svindrych Z, Hagen GM. ThunderSTORM: a comprehensive ImageJ plug-in for PALM and STORM data analysis and super-resolution imaging. *Bioinformatics (Oxford, England)* **30**, 2389-2390 (2014).

66. Andronov L, Lutz Y, Vonesch J-L, Klaholz BP. SharpViSu: integrated analysis and segmentation of super-resolution microscopy data. *Bioinformatics* **32**, 2239-2241 (2016).

67. Möckl L*, et al.* Quantitative Super-Resolution Microscopy of the Mammalian Glycocalyx. *Developmental Cell* **50**, 57-72 (2019).

68. Schwarz G. Estimating the dimension of a model. *The annals of statistics* **6**, 461-464 (1978).

69. Marin Z*, et al.* PYMEVisualize: an open-source tool for exploring 3D super-resolution data. *Nature Methods* **18**, 582-584 (2021).

70. Pedregosa F*, et al.* Scikit-learn: Machine Learning in Python. *J Mach Learn Res* **12**, 2825–2830 (2011).

Supplementary figures

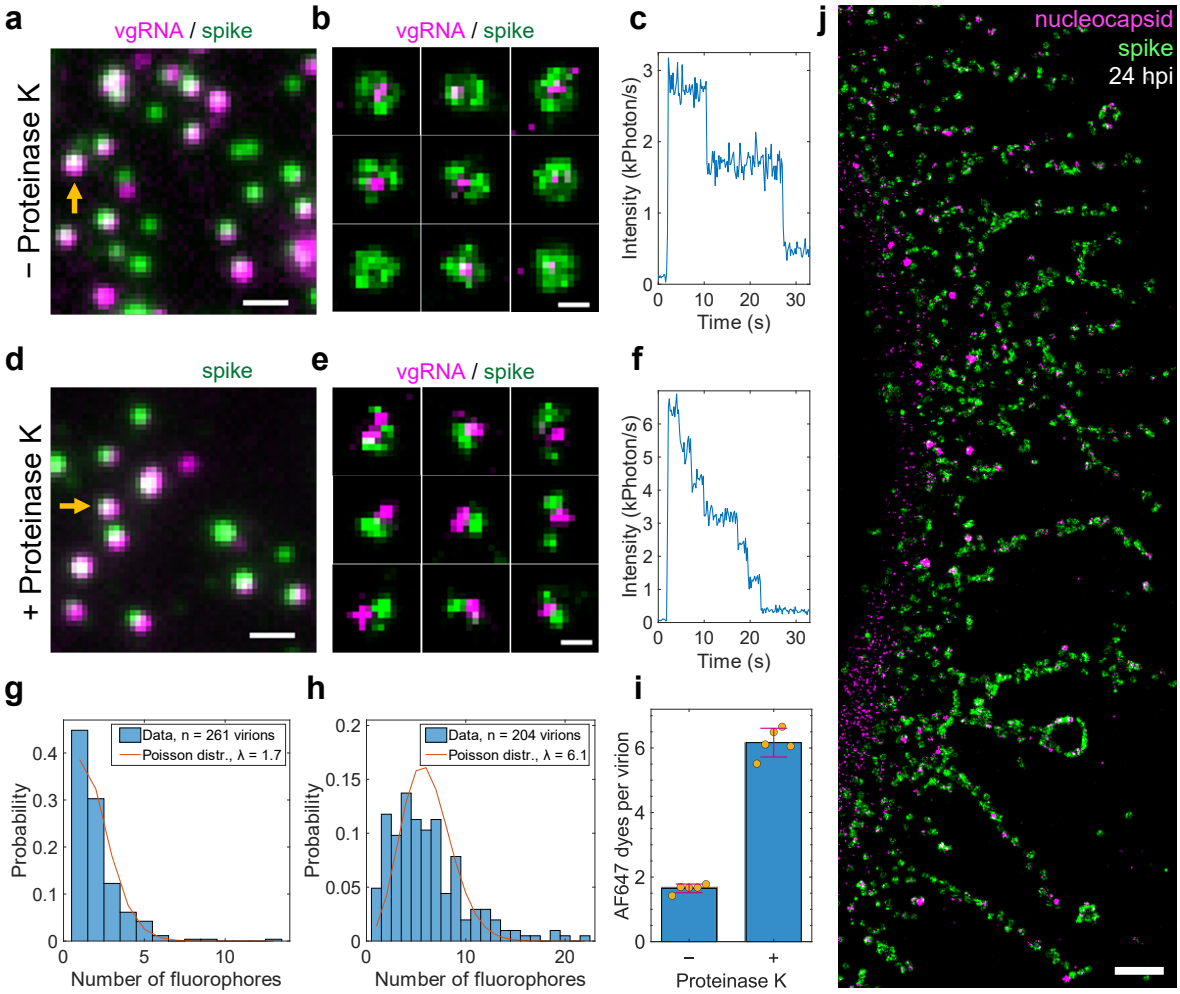

Fig. S1. Validation of the labeling and imaging approach.

a, DL image of SARS-CoV-2 virions where vgRNA was labeled with AF647 by RNA FISH and the spike proteins were labeled by primary anti-spike S2 antibody with secondary CF568-conjugated antibody. **b**, Representative two-color SR images of individual virions reveal concentric localization of spike around vgRNA. **c**, Bleaching time trace of AF647 emission from a single virion (yellow arrow in **a**) demonstrates two-step bleaching. **d**, DL image of virions that were treated with Proteinase K (PK) before labeling. **e**, SR images of PK-treated virions reveal incomplete spike labeling due to digestion of proteins by the PK. **f**, Bleaching time trace of AF647 emission from a single virion (yellow arrow in **d**) shows 6-step bleaching suggesting increased vgRNA labeling efficiency in PK-treated virions. **g**-**h**, Histograms of the number of fluorophores per virion in untreated (**g**) or PK-treated (**h**) samples and their fits with a Poisson distribution. **i**, Mean number of AF647 molecules per virion from the fit for 5 different regions in both untreated and PK-treated samples. p-value = $2 \cdot 10^{-8}$, two-tailed t-test. The error bars indicate mean ± SD value for the untreated and PK-treated groups. **j**, SR image of a SARS-CoV-2 infected cell with the cell body to the left reveals assembled virions at its cytoplasmic tubular projections at 24 hpi. Scale bars, 100 nm (**b**, **e**) and 1 µm (**a**, **d**, **j**).

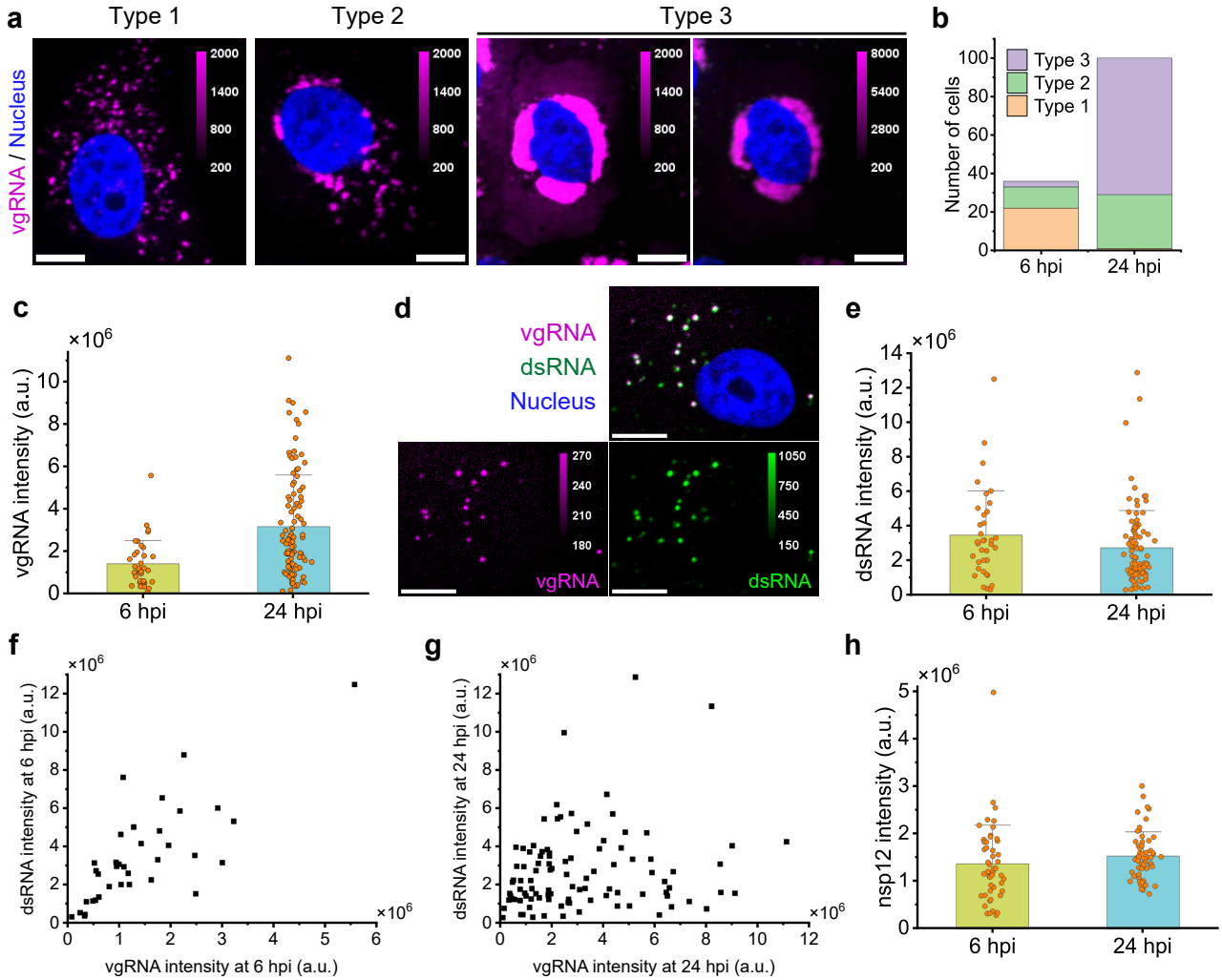

Fig. S2. Screening and quantification of vgRNA, dsRNA and nsp12 by confocal microscopy.

a, Representative confocal images show three types of vgRNA distribution in SARS-CoV-2 infected cells. **b**, Number of cells assigned to one of the three types at 6 or 24 hpi. **c**, Cell-integrated vgRNA signal significantly increases from 6 hpi to 24 hpi. p-value = $6 \cdot 10^{-8}$, two-tailed t-test. **d**, Representative confocal image of vgRNA and dsRNA in an early type 1 cell suggests colocalization between these targets. **e**, Cell-integrated signal of immunofluorescently detected dsRNA in SARS-CoV-2 infected cells does not significantly change from 6 hpi to 24 hpi. p-values = 0.13, two-tailed t-test. **f**, dsRNA signal correlates with vgRNA signal at 6 hpi (Pearson's r = 0.76). **g**, dsRNA signal does not correlate with vgRNA signal at 24 hpi (Pearson's r = 0.18). **h**, Cell-integrated signal of immunofluorescently detected nsp12 in SARS-CoV-2 infected cells does not significantly change from 6 hpi to 24 hpi. p-value = 0.23, two-tailed t-test. Error bars represent mean + SD of the values from individual cells. Scale bars, 10 µm.

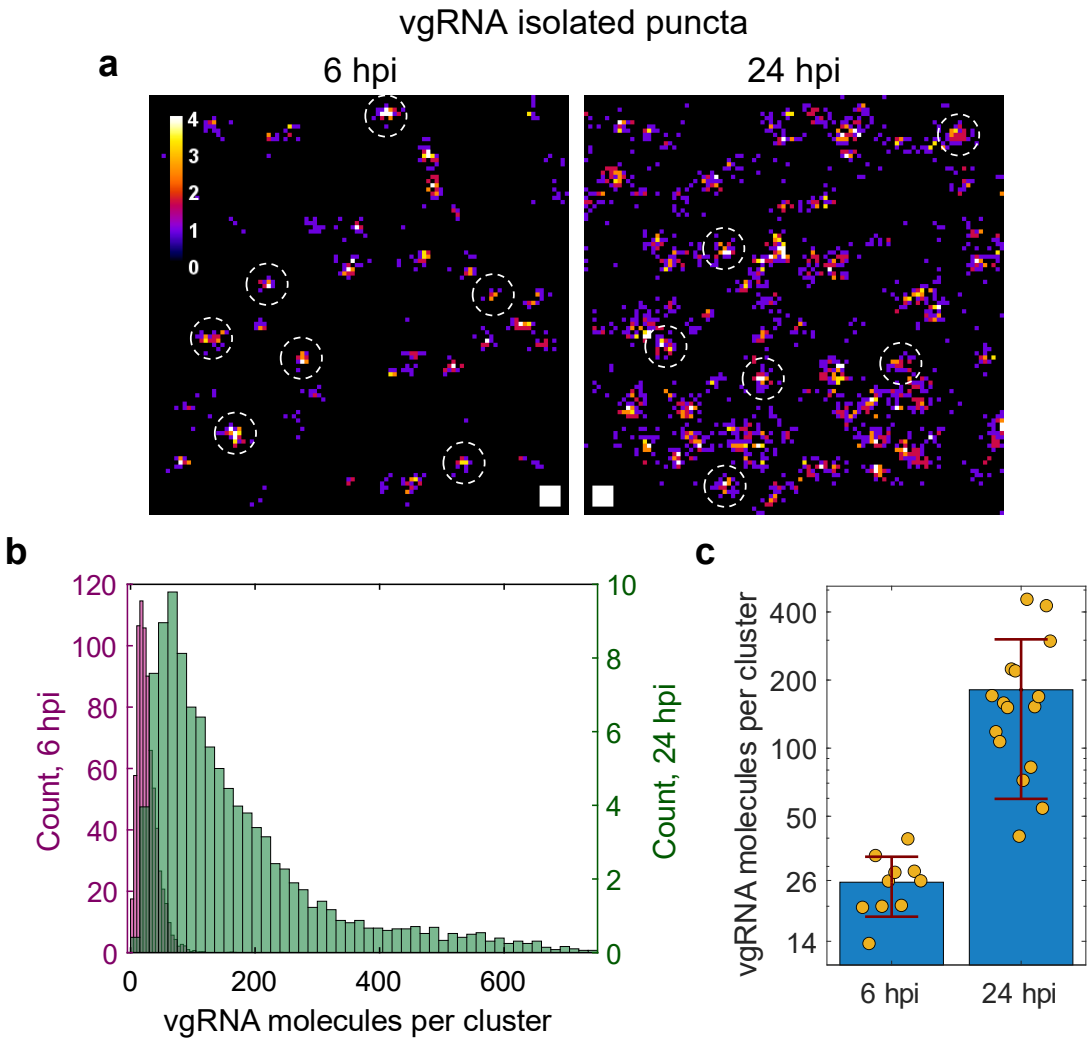

Fig. S3. Estimation of the number of vgRNA molecules in vgRNA clusters.

a, SR localizations of single vgRNA molecules found in the cytoplasm of infected cells outside the dense vgRNA clusters. On a cell-by-cell basis, similar images are used as a calibration for the number of SR detections per one vgRNA molecule. Examples of SR images of single vgRNA molecules are indicated with white circles (r = 50 nm). **b**, Estimated number of vgRNA molecules per cluster at 6 and 24 hpi from all analyzed cells. The histogram counts are normalized by the number of analyzed cells; the histogram counts for 24 hpi were additionally divided by 3 to account for the 3x wider bin size than at 6 hpi. **c**, Median estimated counts of vgRNA molecules per cluster for each analyzed cell (individual yellow points). The error bars represent mean ± SD values of these median vgRNA molecule counts for each time point. P-value = $5 \cdot 10^{-4}$, two-tailed t-test. Scale bars, 50 x 50 nm^2.

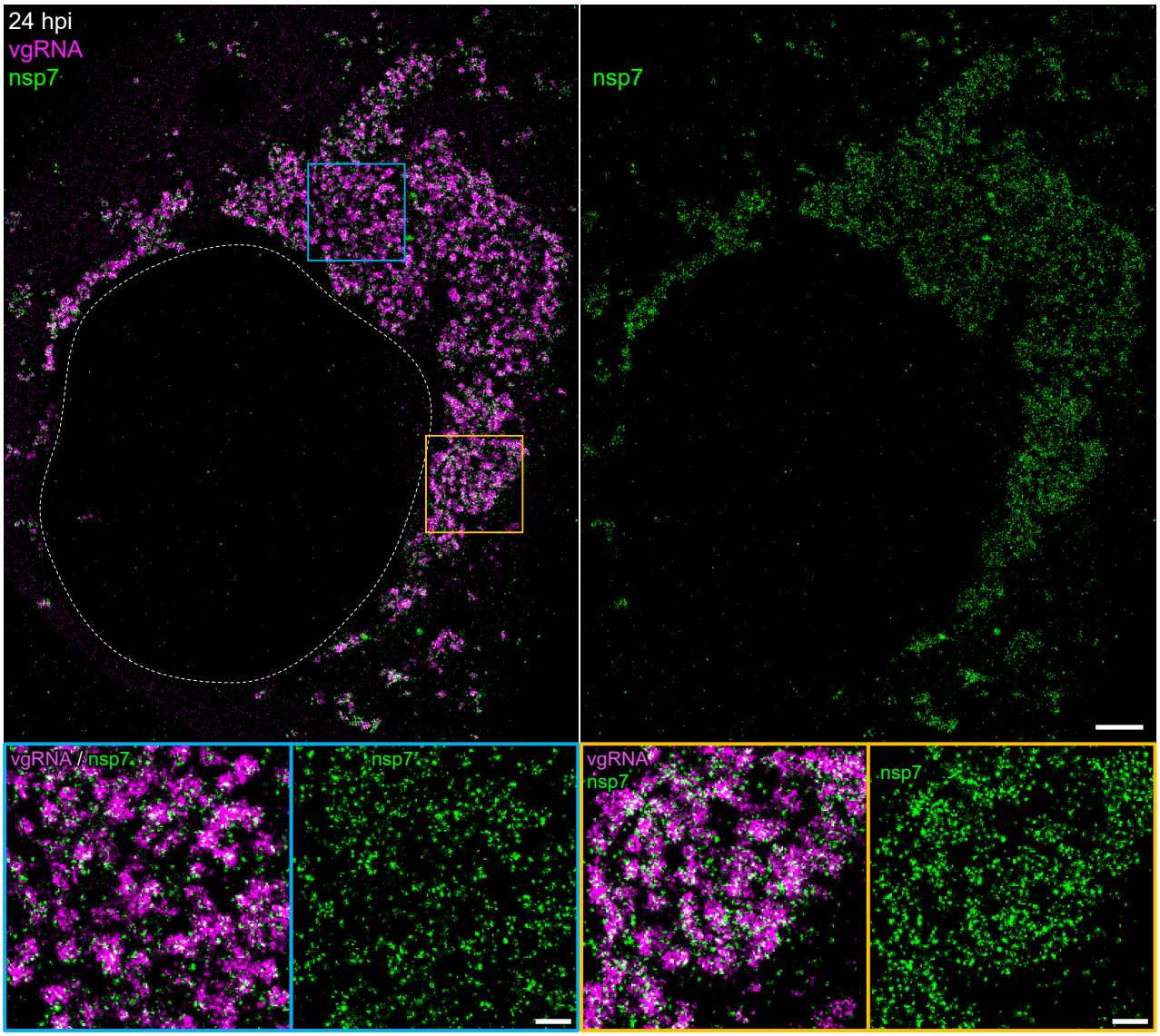

Fig. S4. Association of nsp7 with perinuclear vgRNA structures.

Representative SR image of a SARS-CoV-2 infected cell at 24 hpi labeled for vgRNA (magenta) and nsp7 (green) with magnified regions shown in the colored boxes. Scale bars, 2 µm and 500 nm (bottom panels).

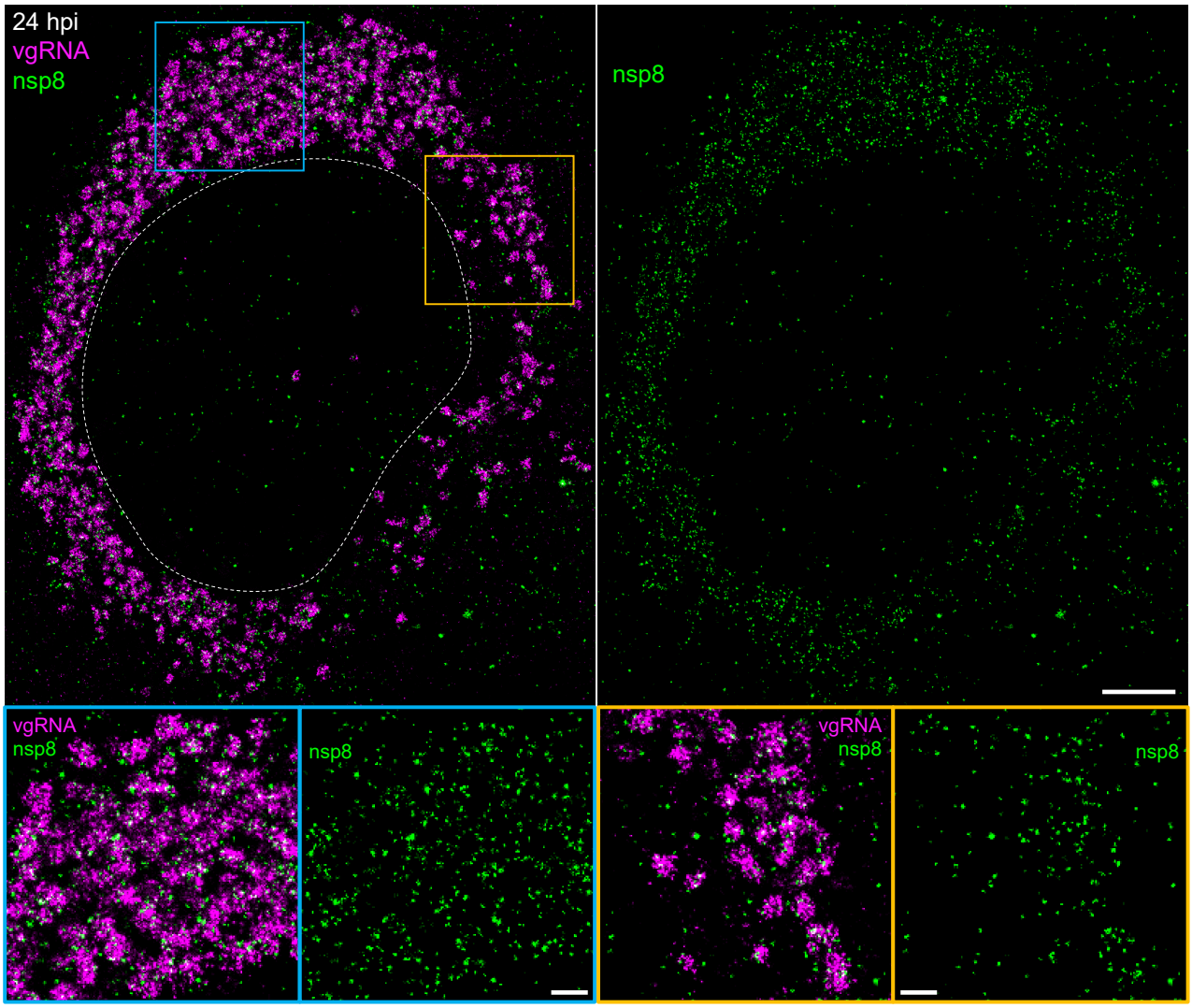

Fig. S5. Association of nsp8 with perinuclear vgRNA structures.

Representative SR image of a SARS-CoV-2 infected cell at 24 hpi labeled for vgRNA (magenta) and nsp8 (green) with magnified regions shown in the colored boxes. Scale bars, 2 µm and 500 nm (bottom panels).

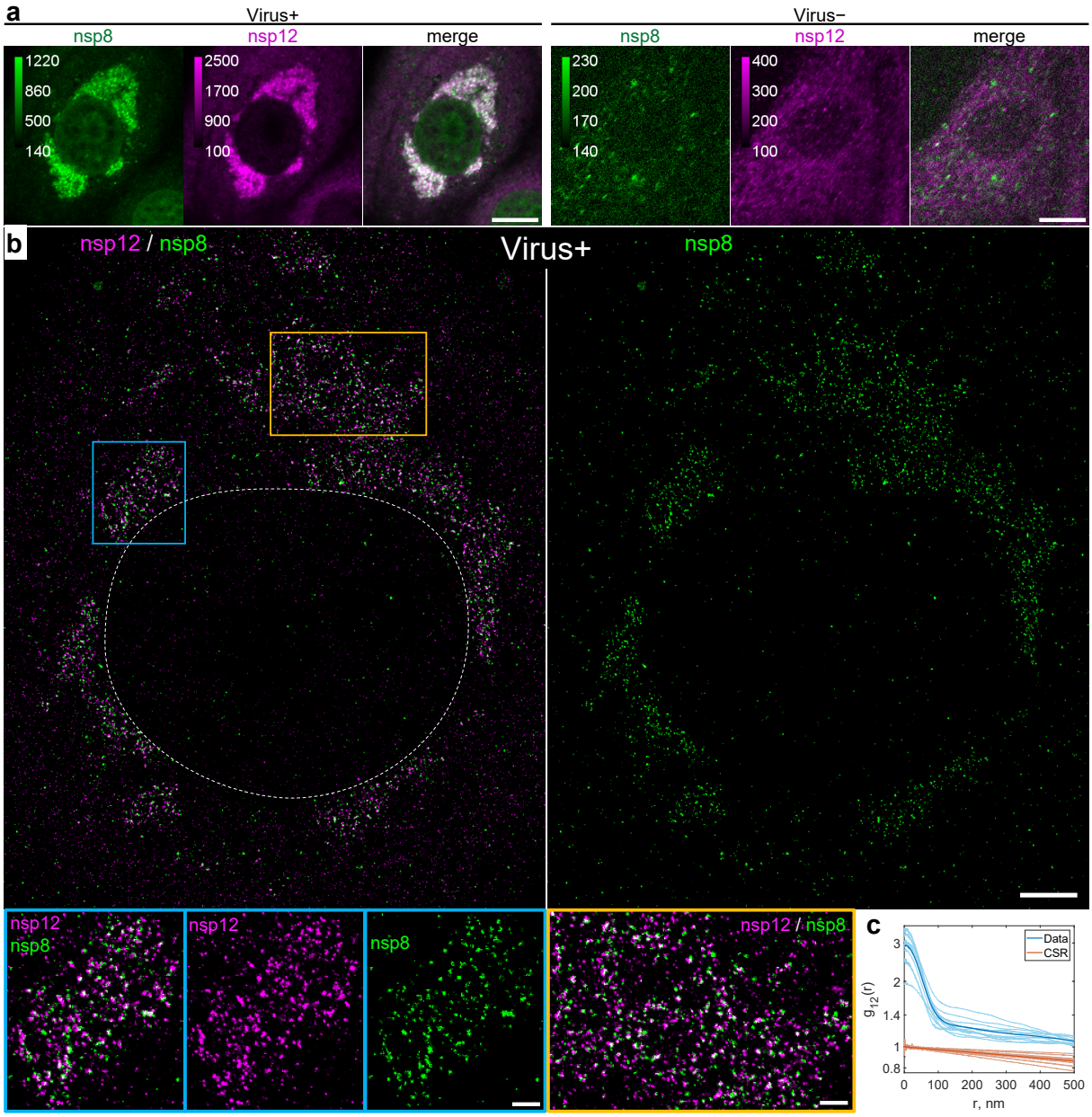

Fig. S6. Colocalization of nsp12 with nsp8.

a, Representative confocal images of cells co-labeled for nsp8 and nsp12 demonstrate their DL colocalization in the perinuclear region of infected cells (Virus+, 24 hpi) and low background immunofluorescence signal in non-infected cells (Virus−). **b**. Representative SR image of an infected cell at 24 hpi reveals punctate localization of both nsp12 and nsp8 in the perinuclear region. (bottom panels) Magnified images of the regions in the colored boxes reveal nanoscale colocalization of nsp12 with nsp8. **c**. Bivariate pair-correlation functions calculated in the perinuclear regions of infected cells demonstrate colocalization of nsp12 and nsp8 at $r < 100$ nm. Scale bars, 10 µm (**a**), 2 µm (**b**) and 500 nm (bottom panels).

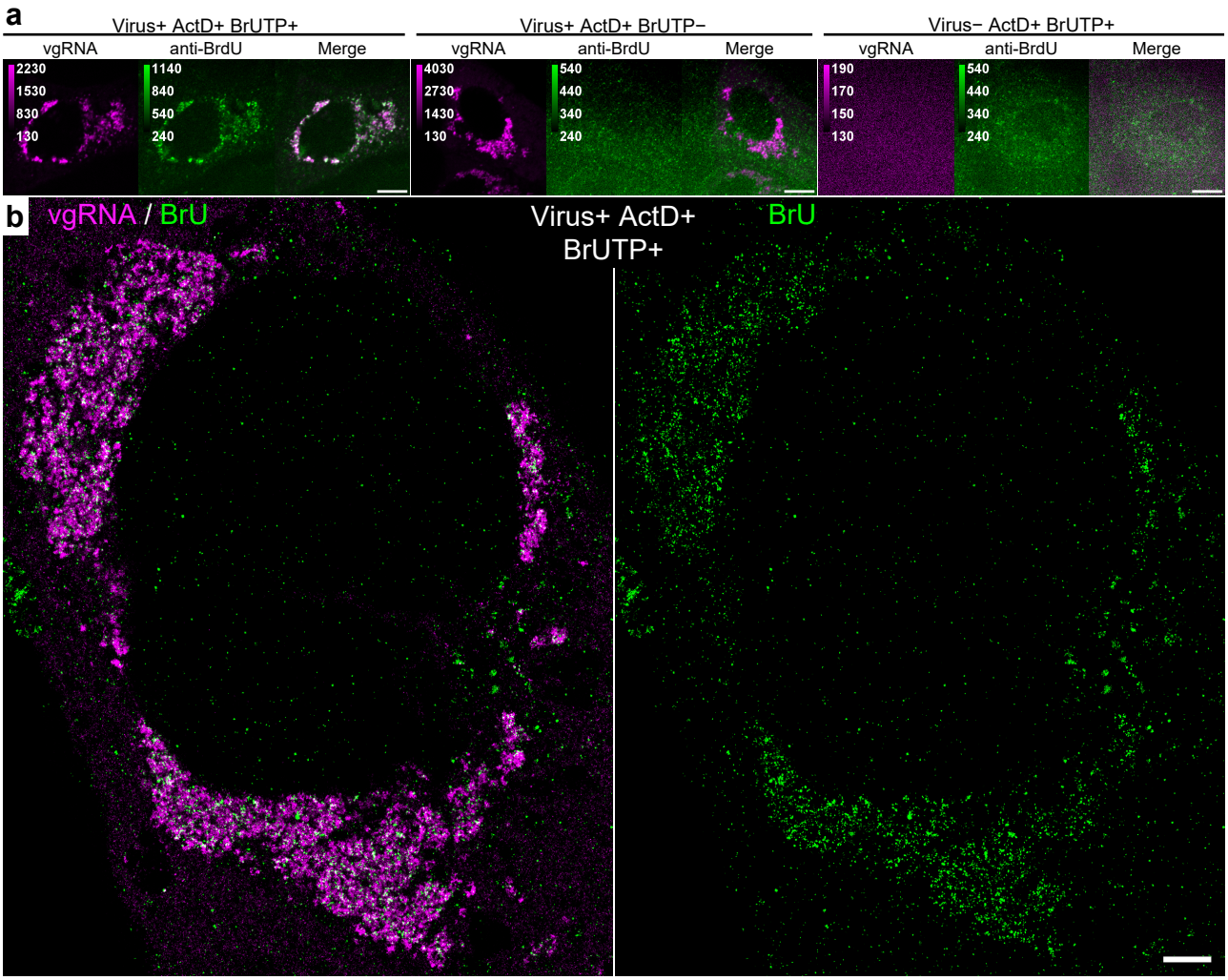

Fig. S7. Association of newly synthesized viral RNAs with perinuclear clusters of vgRNA.

a, Representative confocal images of cells co-labeled for vgRNA and BrU demonstrate their DL colocalization in the perinuclear region of infected cells treated with BrUTP for 1 h before fixation (Virus+ BrUTP+); low background BrU signal in infected cells not treated with BrUTP (Virus+ BrUTP−) and low background signal of both targets in non-infected cells treated with BrUTP for 1 h (Virus− BrUTP+). Endogenous transcription was inhibited with Actinomycin D in all conditions (ActD+). Virus+ cells were fixed at 24 hpi. **b**. Representative SR image of an infected cell at 24 hpi treated with BrUTP and Actinomycin D demonstrates association of BrU labeling with vgRNA clusters. Scale bars, 10 µm (**a**), 2 µm (**b**).

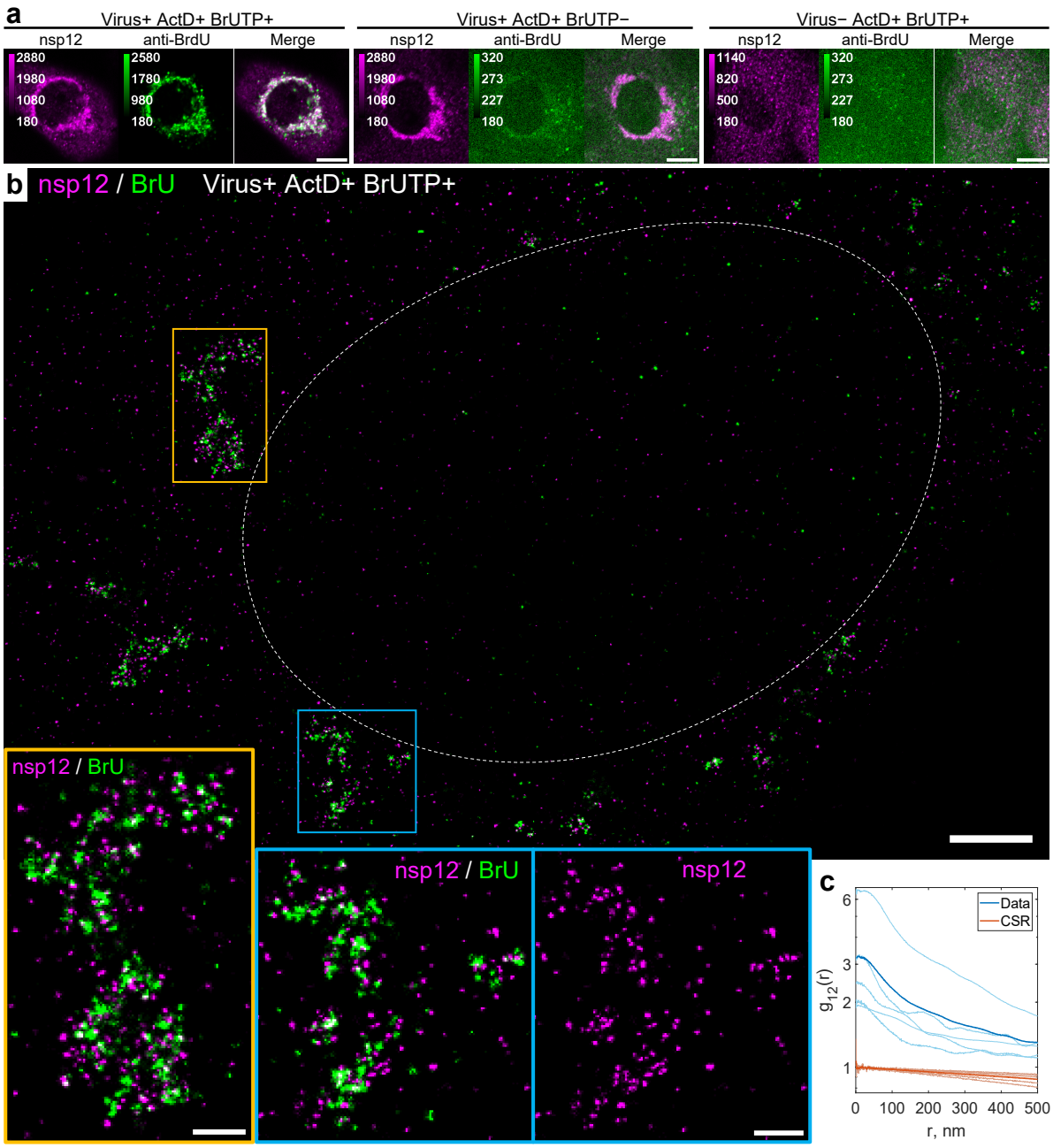

Fig. S8. Association of newly synthesized viral RNAs with nsp12.

a, Representative confocal images of cells co-labeled for nsp12 and BrU demonstrate their DL colocalization in the perinuclear region of infected cells treated with BrUTP for 1 h (Virus+ BrUTP+); low background BrU signal in infected cells not treated with BrUTP (Virus+ BrUTP−); and low background signal of both targets in non-infected cells treated with BrUTP for 1 h (Virus− BrUTP+). Endogenous transcription was inhibited with Actinomycin D in all conditions (ActD+). Virus+ cells were fixed at 24 hpi. **b**. SR image of an infected cell (type 1, early infection) treated with BrUTP demonstrates association of BrU labeling with nsp12. **c**. Bivariate pair-correlation functions calculated in the perinuclear regions of infected and BrUTP-treated cells reveal nanoscale association of nsp12 and BrU. Scale bars, 10 µm (**a**), 2 µm (**b**) and 500 nm (bottom zoomed-in panels).

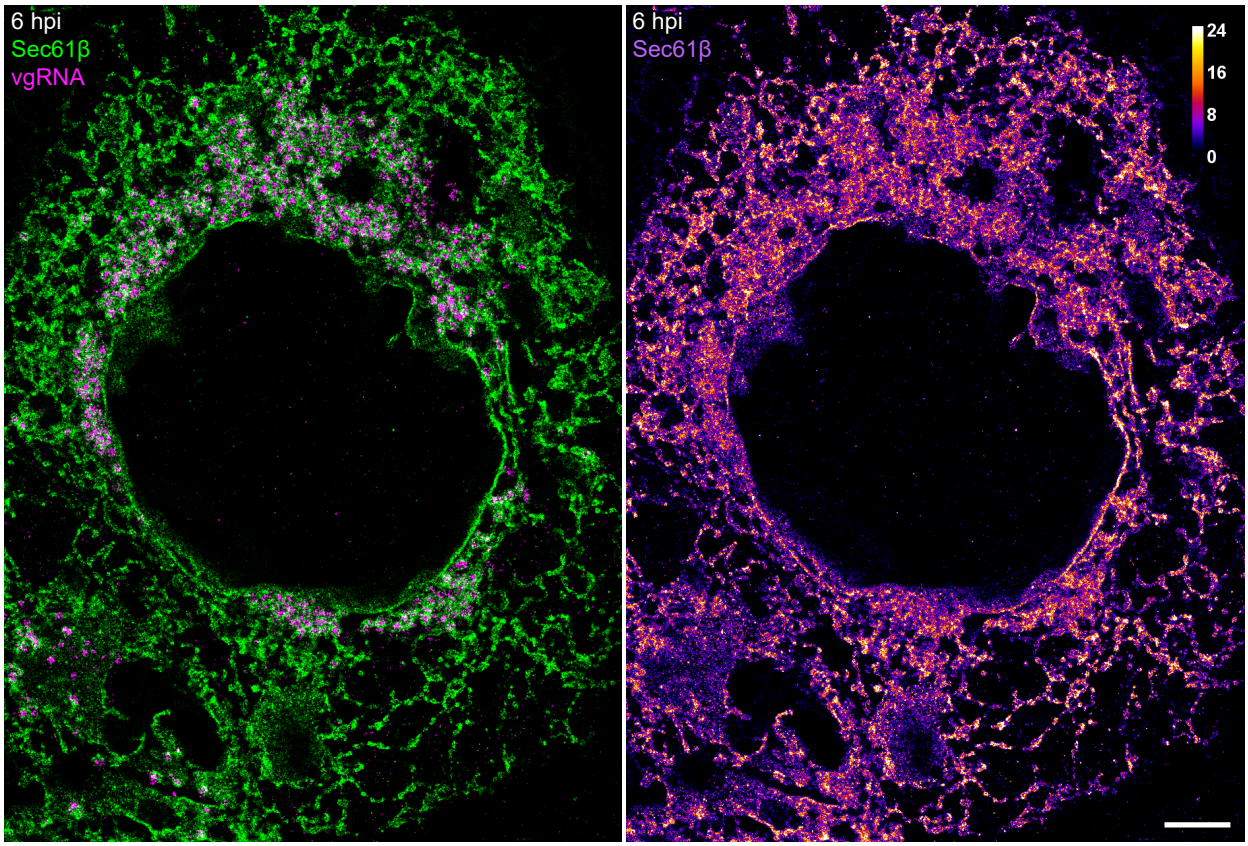

Fig. S9. Alterations of host cell ER at 6 hpi.

SR image of vgRNA in a SARS-CoV-2 infected Vero E6 cell, stably expressing Sec61β-GFP. Altered ER forms ring-like structures that partially encapsulate vgRNA clusters in the perinuclear region. Left: green (Sec61β) / magenta (vgRNA) coloring; right: color scale of Sec61β localizations. Scale bar, 2 µm.

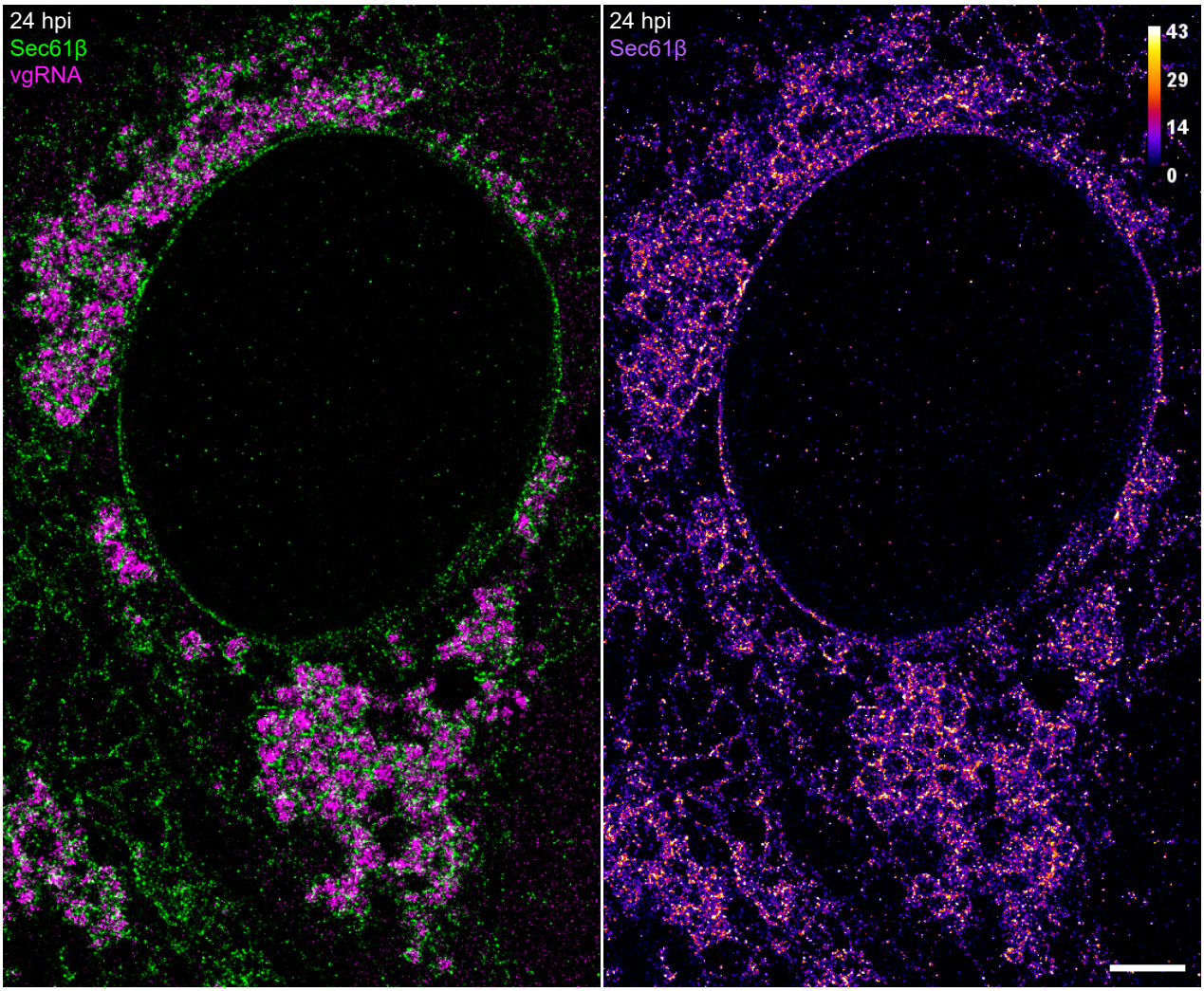

Fig. S10. Alterations of host cell ER at 24 hpi.

SR image of vgRNA in a SARS-CoV-2 infected Vero E6 cell, stably expressing Sec61β-GFP. Altered ER forms ring-like structures that encapsulate vgRNA clusters in the perinuclear region, while the Sec61β signal at the ER tubules decreases compared to 6 hpi (Fig. S9). Left: green (Sec61β) / magenta (vgRNA) coloring; right: color scale of Sec61β localizations. Scale bar, 2 µm.

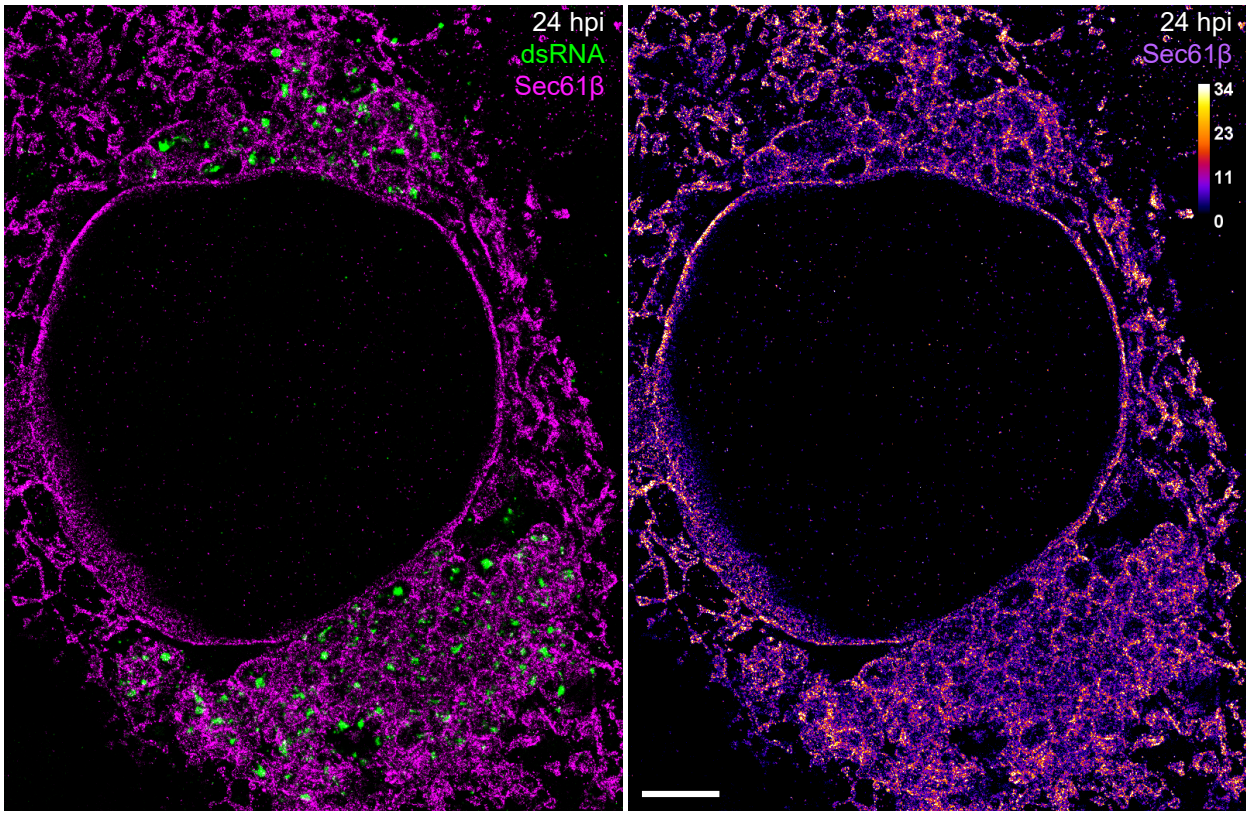

Fig. S11. Encapsulation of dsRNA by altered host ER at 24 hpi.

SR image of dsRNA in a SARS-CoV-2 infected Vero E6 cell, stably expressing Sec61β-GFP. Ring-like structures of altered ER encapsulate dsRNA clusters in the perinuclear region. Left: green (dsRNA) / magenta (Sec61β) coloring; right: color scale of Sec61β localizations. Scale bar, 2 µm.

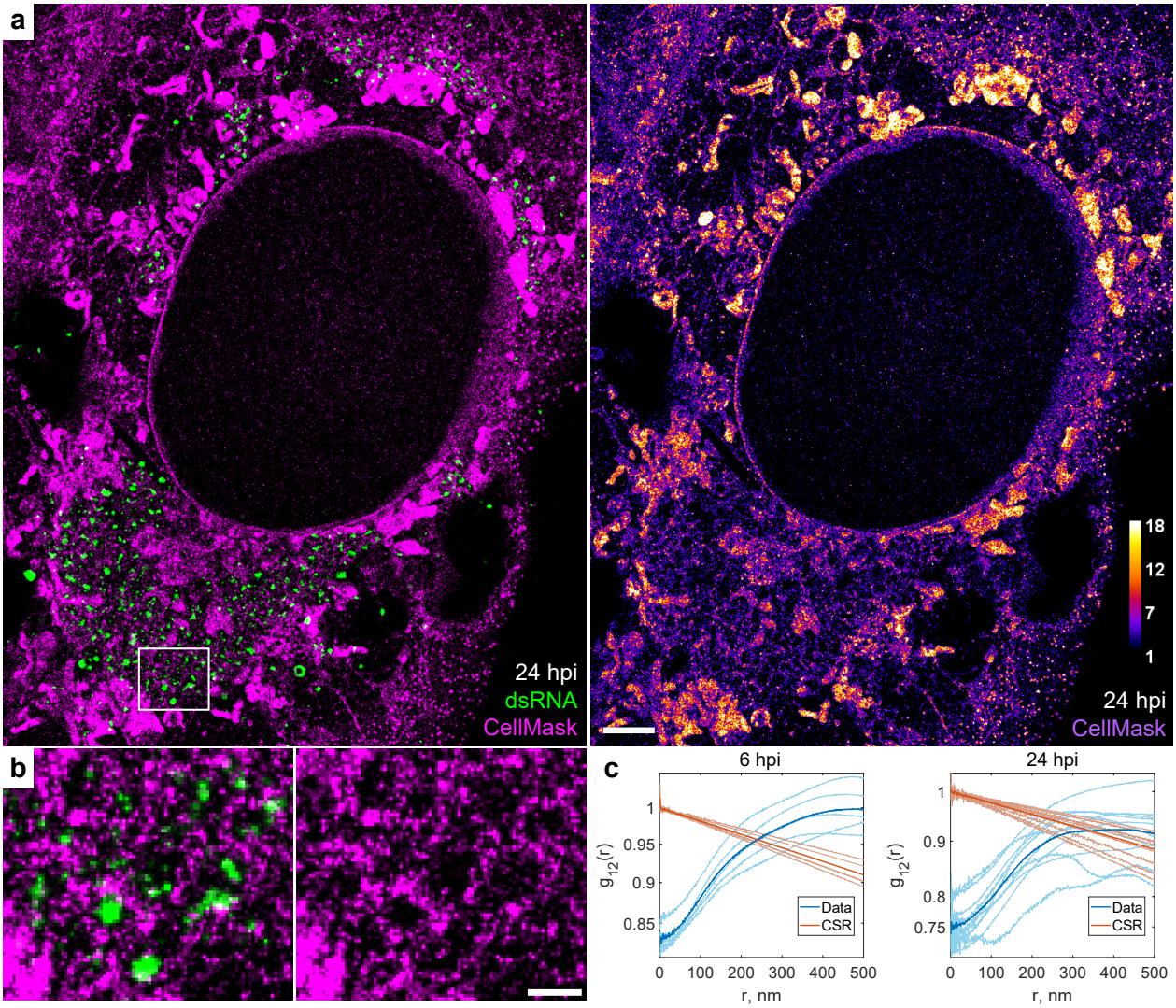

Fig. S12. Encapsulation of dsRNA into membrane-bound organelles.

a, SR image of dsRNA and membranes in a SARS-CoV-2 infected cell at 24 hpi with membranes labeled by CellMask Deep Red (magenta) and dsRNA labeled with immunofluorescence (green). CellMask-labeled membranes can be observed around dsRNA clusters. Virions at the plasma membrane are seen as bright puncta (right side and lower right corner of the image). **b**, Zoomed-in image that corresponds to the white box in **a**. **c**, Bivariate pair-correlation functions indicate nanoscale anti-correlation between dsRNA and CellMask, consistent with dsRNA encapsulation in membrane-bound organelles at both 6 and 24 hpi. Scale bars, 2 µm (**a**) and 500 nm (**b**).

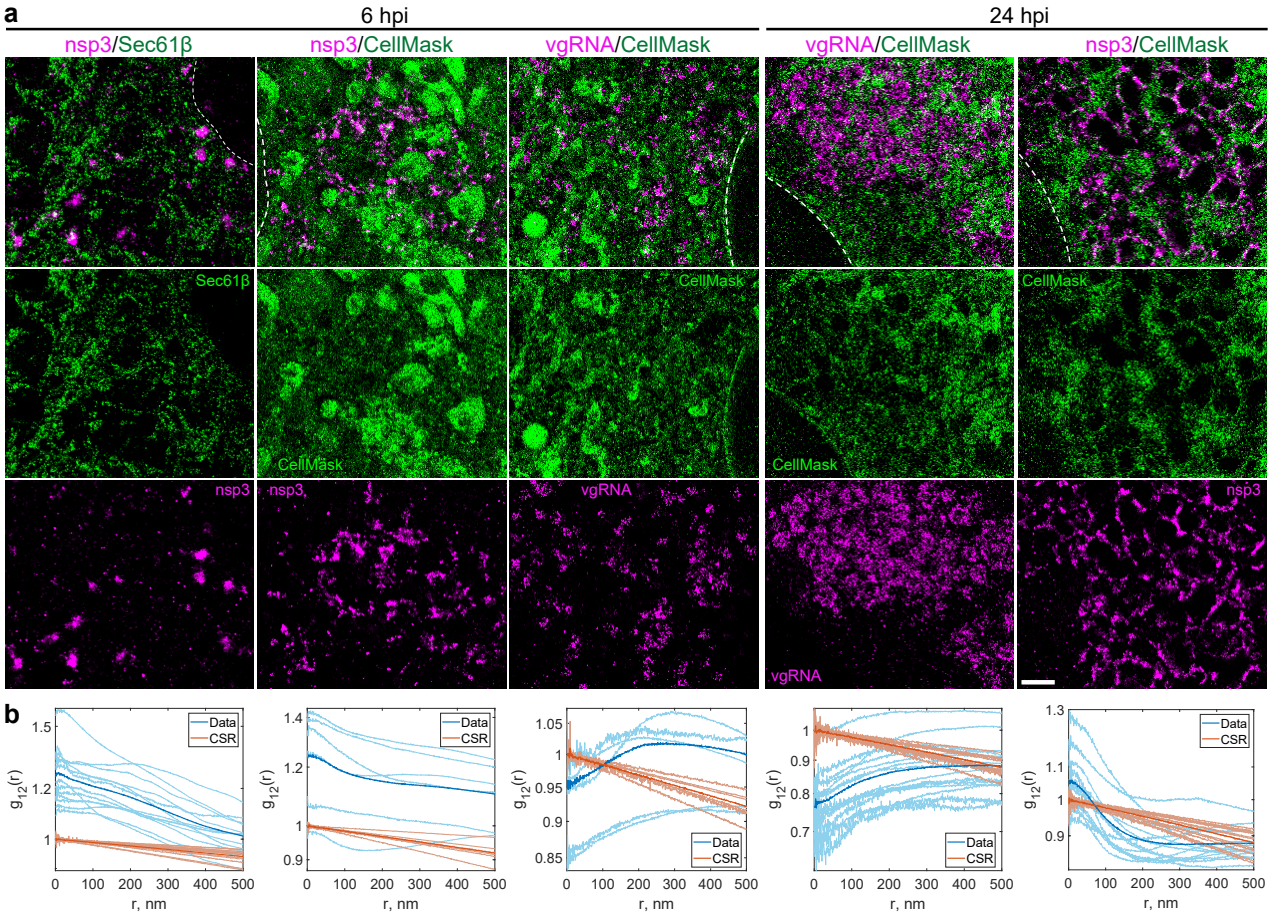

Fig. S13. Nanoscale co-organization of viral components with host cell membranes.

a, SR images of nsp3, Sec61β, vgRNA and membranes (CellMask) in SARS-CoV-2 infected cells at 6 and 24 hpi. **b**, Bivariate pair-correlation functions indicate nanoscale association between nsp3 and Sec61β, nsp3 and CellMask, and nanoscale anti-correlation between vgRNA and CellMask at both time points. Scale bar, 1 µm.

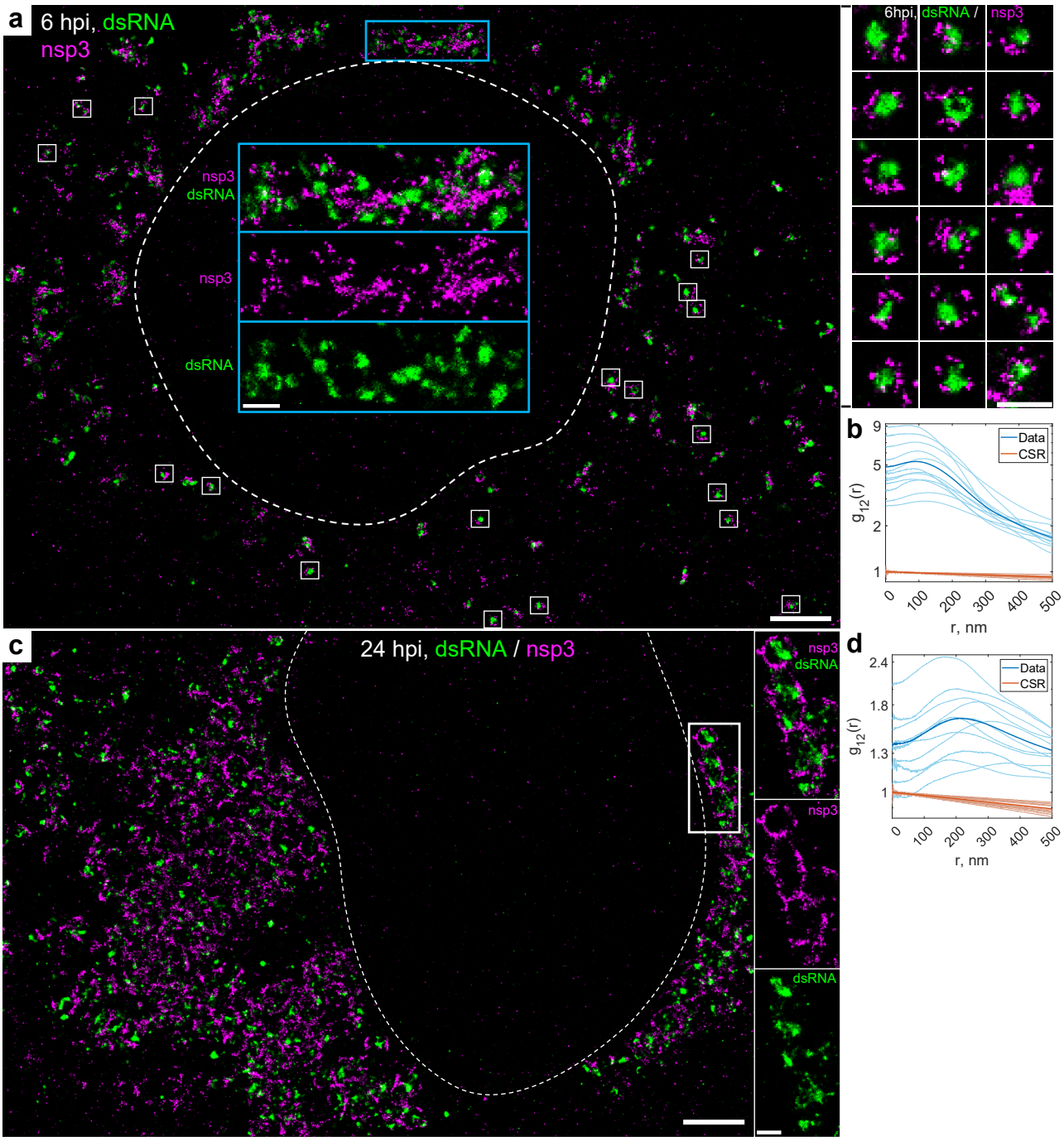

Fig. S14. Nanoscale anti-correlation of nsp3 with dsRNA.

a, SR image of a SARS-CoV-2 infected cell at 6 hpi with nsp3 and dsRNA labeled by immunofluorescence. Nsp3 can be observed at the surface of isolated dsRNA clusters (white boxes & right panel) or in dense aggregates between dsRNA clusters (blue box & blue insets). **b**, Bivariate pair-correlation functions indicate nanoscale anti-correlation between dsRNA and nsp3 at 6 hpi. **c**, SR image of a SARS-CoV-2 infected cell at 24 hpi. Nsp3 forms a network-like pattern that encapsulates dsRNA clusters. **d**, Bivariate pair-correlation functions indicate nanoscale anti-correlation between dsRNA and nsp3 at 24 hpi. Scale bars, 2 µm (**a**, **c**) and 500 nm (insets in **a**, **c** and right panel in **a**).

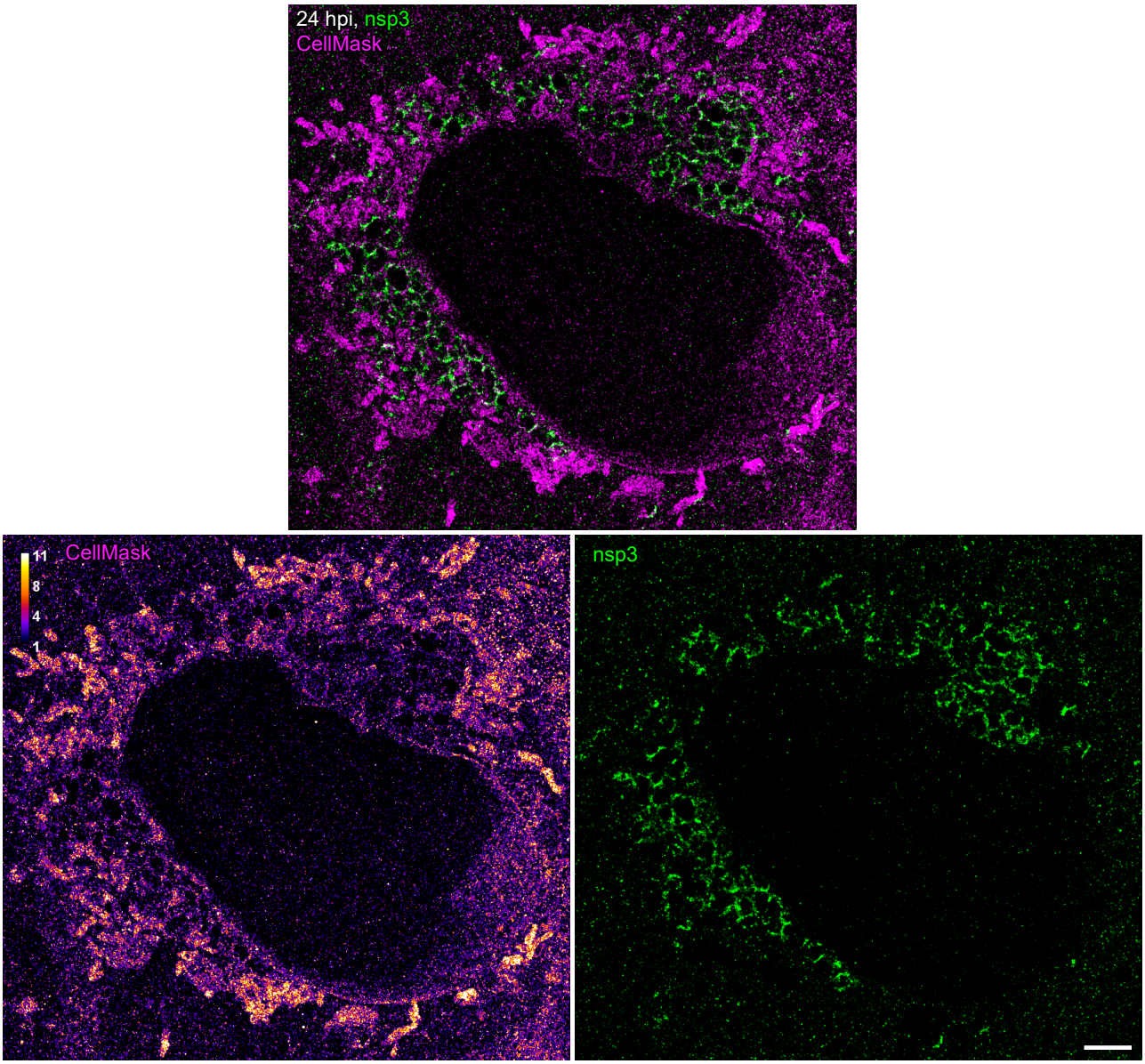

Fig. S15. Nanoscale colocalization of nsp3 with membranes at 24 hpi.

SR image of nsp3 (green) and membranes as labeled by CellMask (magenta) in SARS-CoV-2 infected cells at 24 hpi. Nsp3 forms a network-like pattern in the perinuclear region that colocalizes with the CellMask pattern. Scale bar, 2 µm.

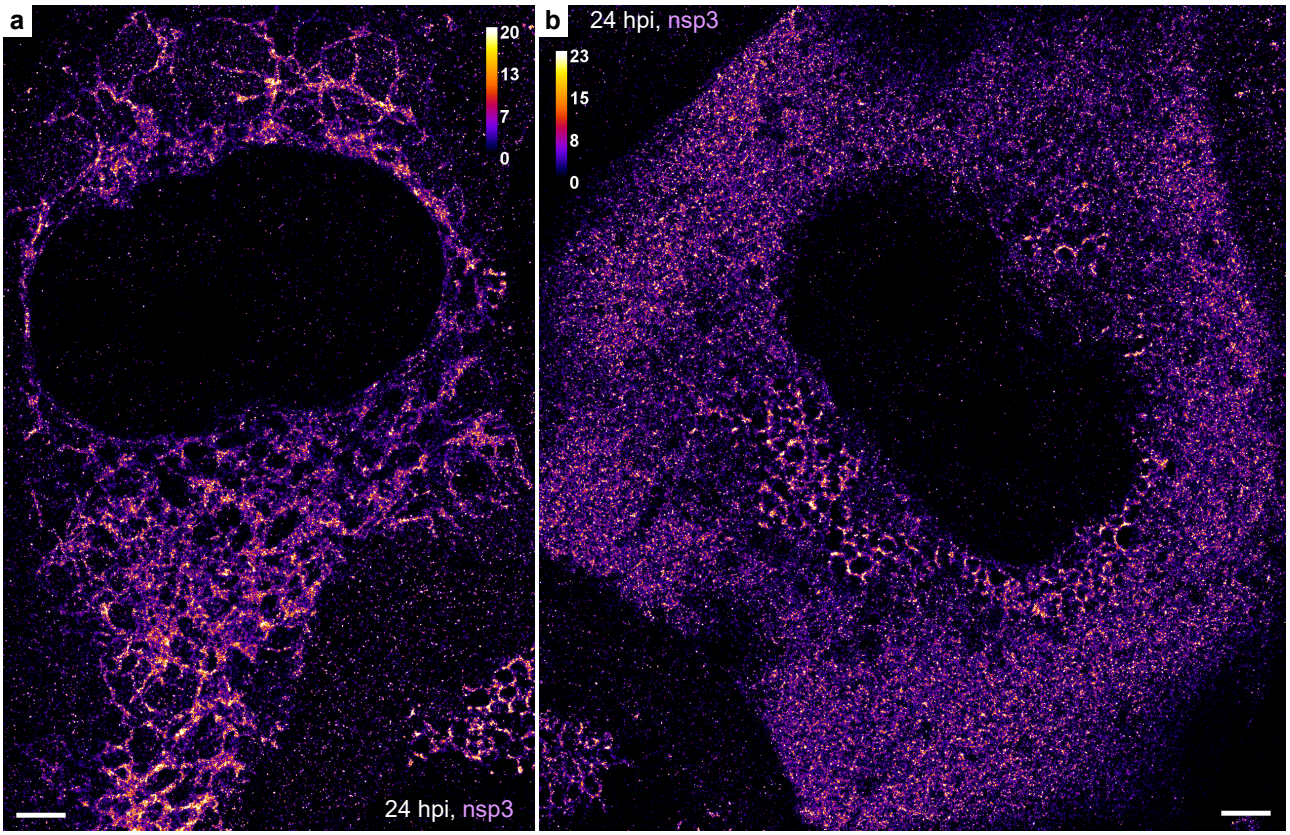

Fig. S16. Less common patterns of nanoscale nsp3 localization at 24 hpi.

a, Nsp3 forms an ER-like network that occupies a large part of the cytoplasm. **b**, Besides the common perinuclear pattern, Nsp3 is also diffusely localized throughout the whole cytoplasm. Scale bars, 2 µm.

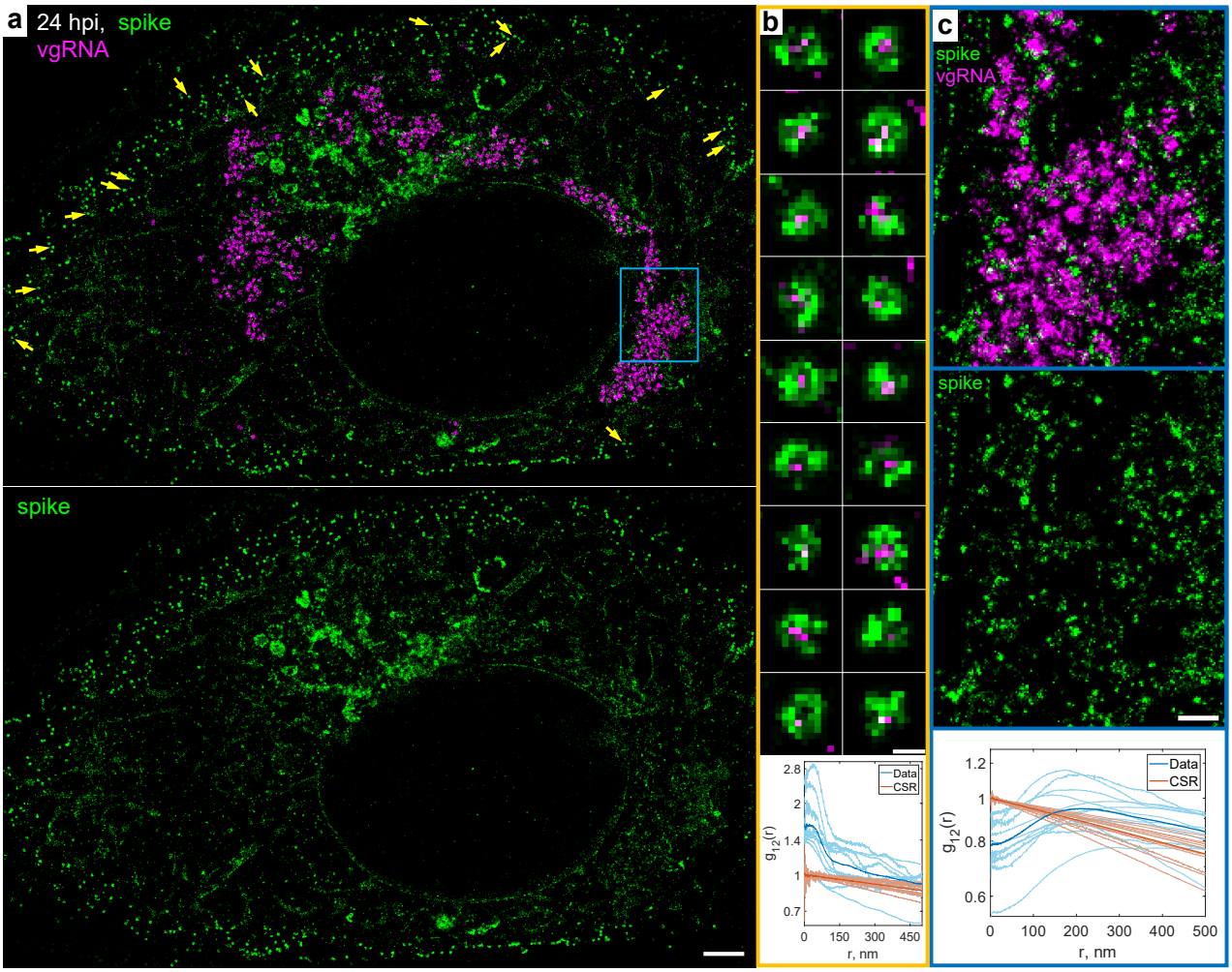

Fig. S17. Nanoscale localization of spike protein at 24 hpi.

a, SR image of a SARS-CoV-2 infected cell at 24 hpi labeled for spike (green) and vgRNA (magenta). **b**, Examples of assembled virions encapsulated by the spike proteins and with vgRNA in their interior, detected at the cell periphery (yellow arrows in **a**). (bottom panel) Bivariate pair-correlation functions calculated in the plasma membrane regions indicate colocalization of these targets at r < 100 nm. **c**, Magnified image that corresponds to the blue frame in **a** displays spike localizations mostly excluded from the interior of the perinuclear vgRNA clusters with possible localization at their membrane. (bottom panel) Bivariate pair-correlation functions calculated in the perinuclear regions of infected cells indicate nanoscale anti-correlation of spike with SARS-CoV-2 replication organelles. Scale bars, 2 µm (**a**), 100 nm (**b**), 500 nm (**c**).

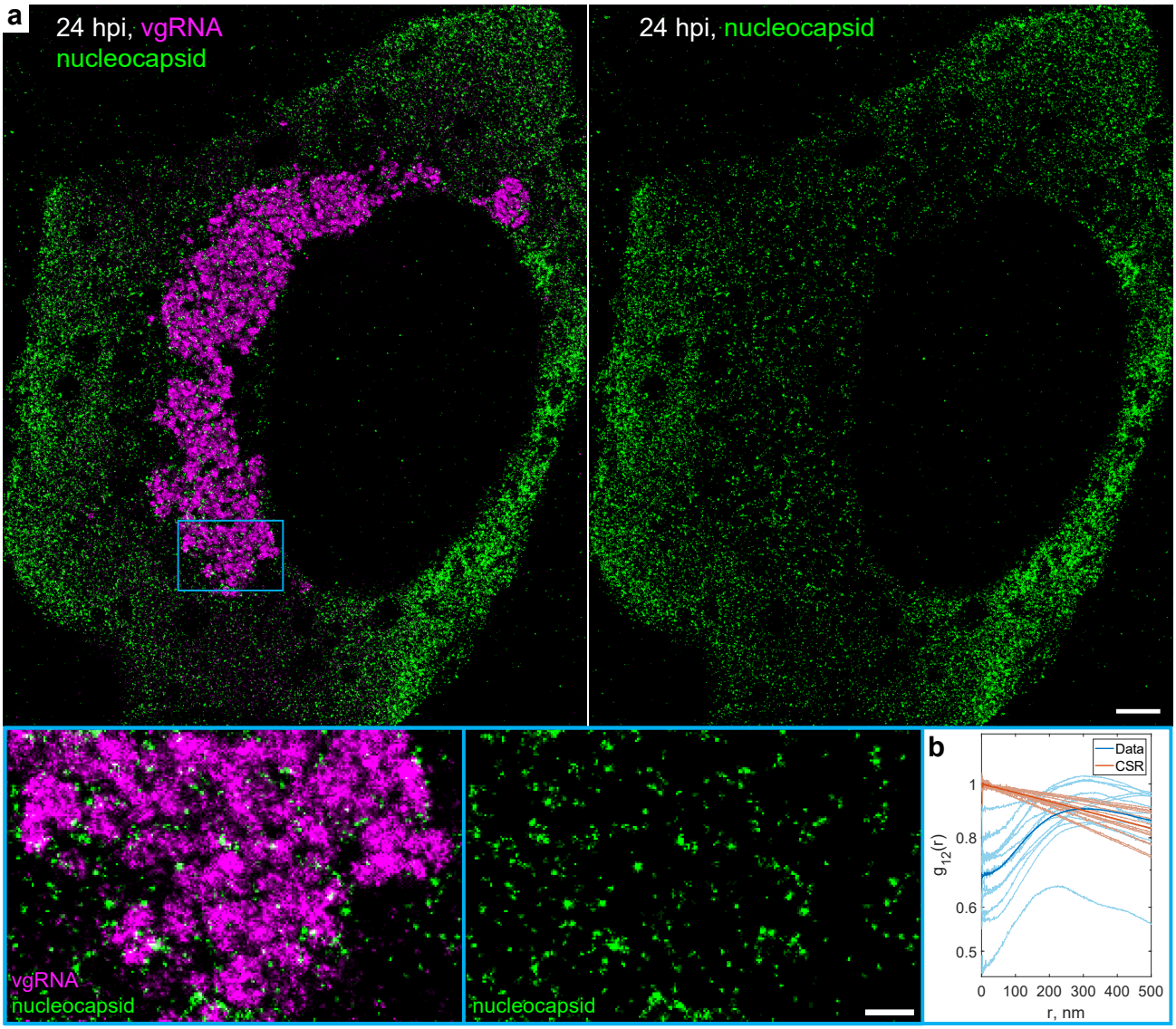

Fig. S18. Nanoscale anti-correlation of nucleocapsid protein with SARS-CoV-2 replication organelles at 24 hpi.

a, SR image of a SARS-CoV-2 infected cell at 24 hpi labeled for the nucleocapsid protein (green) and vgRNA (magenta). The magnified image in the blue frame displays nucleocapsid protein localizations mostly excluded from the interior of the perinuclear vgRNA clusters with possible localization at their membrane. **b**, Bivariate pair-correlation functions calculated in the perinuclear regions of the infected cells indicate nanoscale anti-correlation of the nucleocapsid protein with vgRNA. Scale bars, 2 µm and 500 nm (bottom panels).

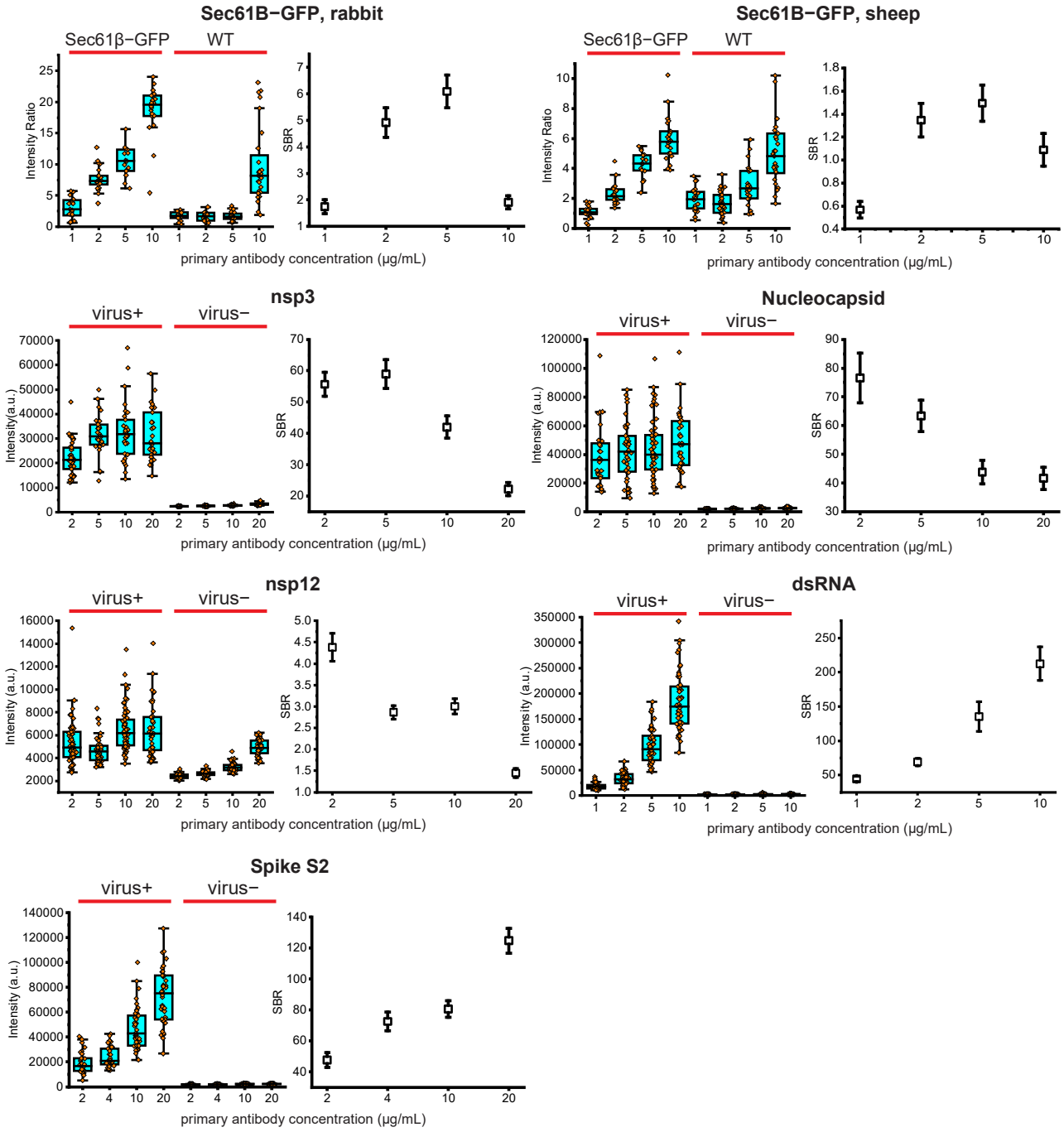

Fig. S19. Optimization of primary antibody concentrations.

The concentration of primary antibodies was optimized to minimize the background or to maximize the signal to background ratio (SBR) between SARS-CoV-2 infected and non-infected cells or between cells expressing Sec61β-GFP and WT cells (see Methods). Box plots: center line, median; box limits, upper and lower quartiles; whiskers, 1.5x interquartile range; dots, values for individual cells. SBR plots show mean ± SD.

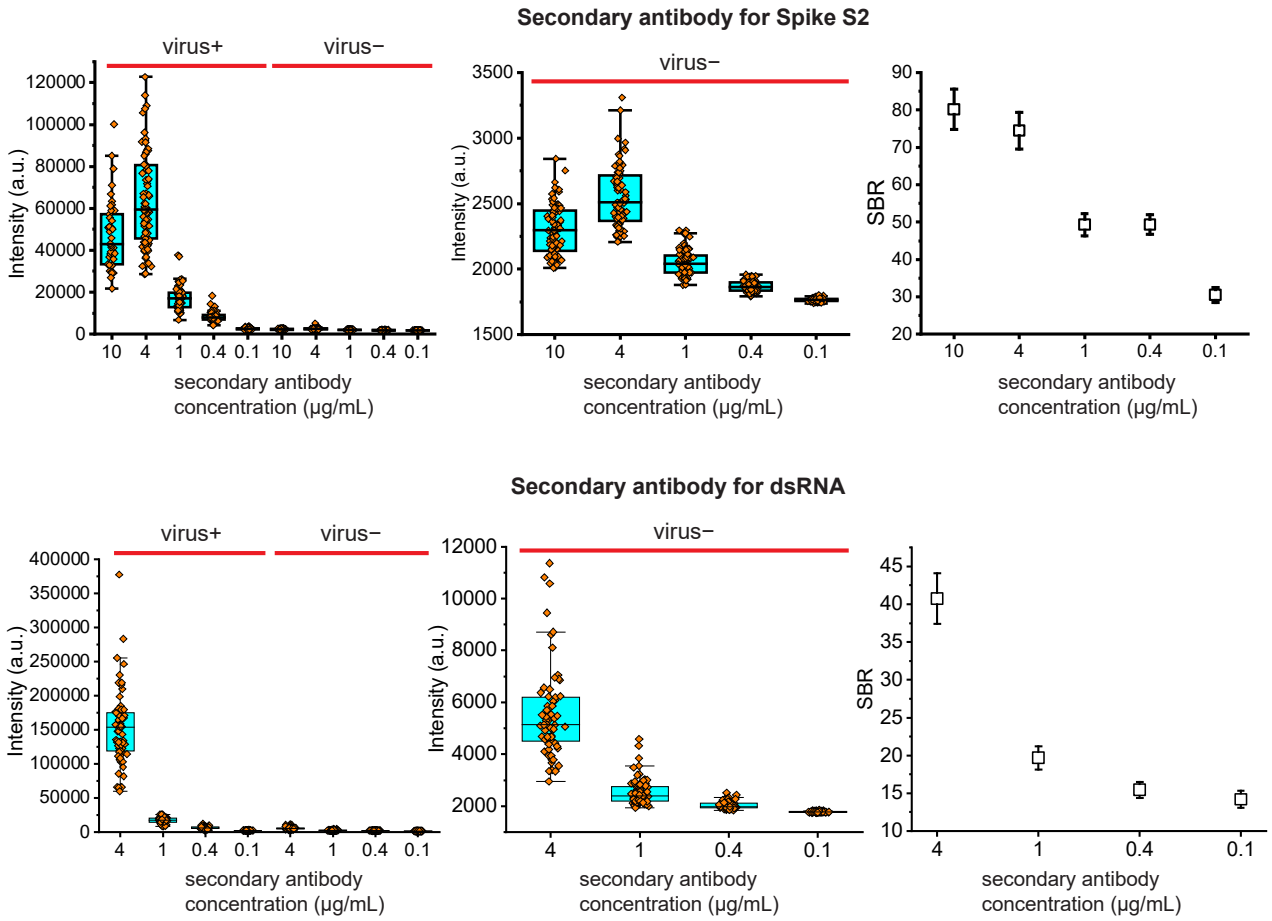

Fig. S20. Optimization of secondary antibody concentrations.

The concentration of secondary antibodies was optimized to minimize the background or to maximize the SBR between SARS-CoV-2 infected and non-infected cells (see Methods). Box plots: center line, median; box limits, upper and lower quartiles; whiskers, 1.5x interquartile range; dots, values for individual cells. SBR plots show mean ± SD.

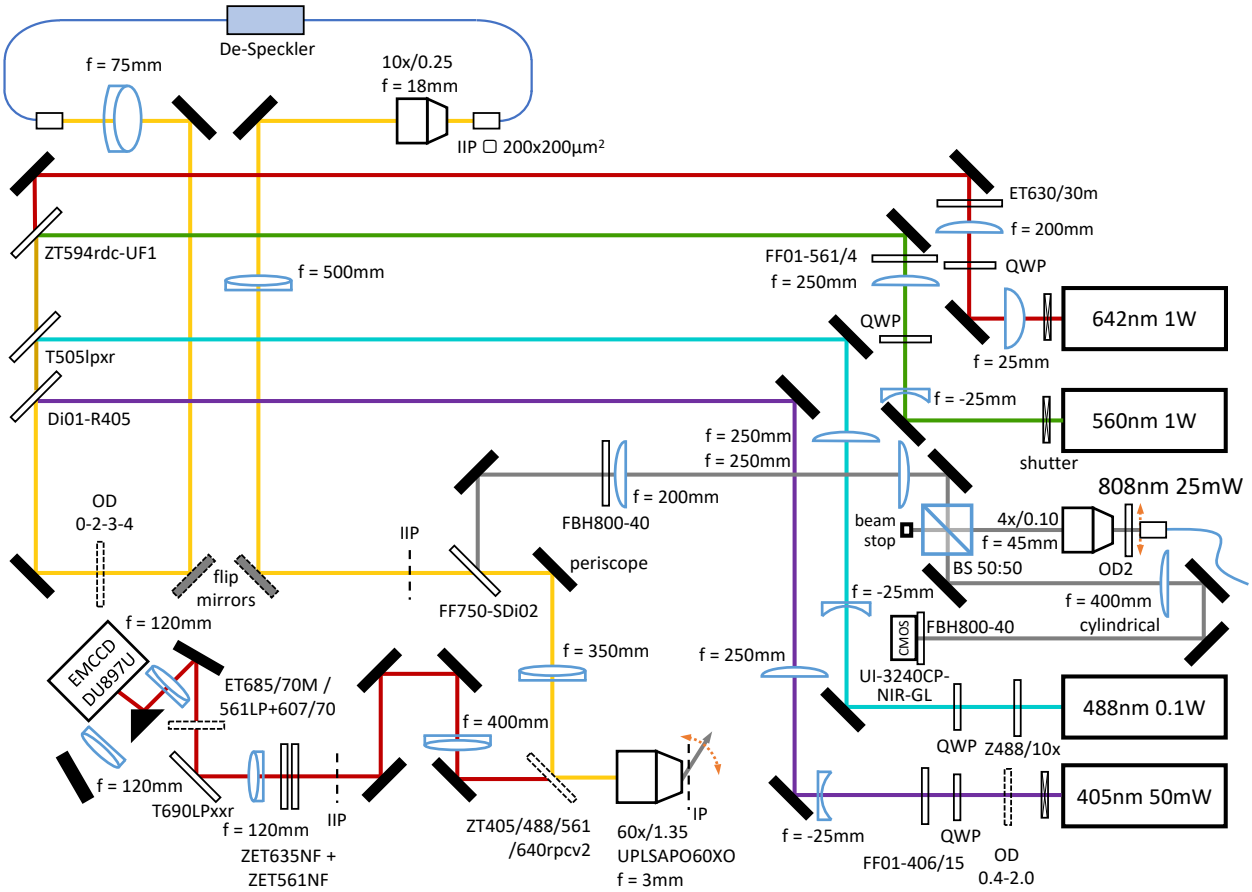

Fig. S21. Path diagram of SR microscope used in this study.

Black-filled icons: mirrors; thin empty rectangles: dichroic or neutral density filters; dashed rectangles: movable or motorized components; boxes: cameras or lasers; bent lines: optical fiber; icons with blue edges: lenses or a beam splitter cube; QWP: quarter-wave plate; IP: image plane; IIP: intermediate image plane; BS: beam splitter; OD: optical density. Optics are shown for producing a second image on the EMCCD, but the second path was not used in this study. The gray lines denote the 808 nm beam in the focus lock apparatus.